

# The High Energy view of the Broad Line Radio Galaxy 3C 111

L. Ballo<sup>1\*</sup>, V. Braito<sup>2</sup>, J. N. Reeves<sup>3</sup>, R. M. Sambruna<sup>4</sup>, and F. Tombesi<sup>5,6</sup><sup>1</sup> Instituto de Física de Cantabria (CSIC-UC), Avda. Los Castros s/n (Edif. Juan Jordá), E-39005 Santander, Spain<sup>2</sup> Department of Physics and Astronomy, University of Leicester, University Road, Leicester LE1 7RH, UK<sup>3</sup> Astrophysics Group, School of Physical and Geographical Sciences, Keele University, Keele, Staffordshire ST5 5BG, UK<sup>4</sup> Department of Physics and Astronomy, MS 3F3, 4400 University Drive, George Mason University, Fairfax, VA 22030, USA<sup>5</sup> X-ray Astrophysics Laboratory and CRESST, NASA/Goddard Space Flight Center, Greenbelt, MD 20771, USA<sup>6</sup> Department of Astronomy, University of Maryland, College Park, MD 20742, USA

Accepted 2011 August 12. Received 2011 August 11; in original form 2011 May 24

## ABSTRACT

We present the analysis of *Suzaku* and *XMM-Newton* observations of the broad-line radio galaxy (BLRG) 3C 111. Its high energy emission shows variability, a harder continuum with respect to the radio quiet AGN population, and weak reflection features. *Suzaku* found the source in a minimum flux level; a comparison with the *XMM-Newton* data implies an increase of a factor of 2.5 in the 0.5 – 10 keV flux, in the 6 months separating the two observations. The iron K complex is detected in both datasets, with rather low equivalent width(s). The intensity of the iron K complex does not respond to the change in continuum flux. An ultra-fast, high-ionization outflowing gas is clearly detected in the XIS data; the absorber is most likely unstable. Indeed, during the *XMM-Newton* observation, which was 6 months after, the absorber was not detected. No clear roll-over in the hard X-ray emission is detected, probably due to the emergence of the jet as a dominant component in the hard X-ray band, as suggested by the detection above  $\sim 100$  keV with the GSO on-board *Suzaku*, although the present data do not allow us to firmly constrain the relative contribution of the different components. The fluxes observed by the  $\gamma$ -ray satellites *CGRO* and *Fermi* would be compatible with the putative jet component if peaking at energies  $E \sim 100$  MeV. In the X-ray band, the jet contribution to the continuum starts to be significant only above 10 keV. If the detection of the jet component in 3C 111 is confirmed, then its relative importance in the X-ray energy band could explain the different observed properties in the high-energy emission of BLRGs, which are otherwise similar in their other multiwavelength properties. Comparison between X-ray and  $\gamma$ -ray data taken at different epochs suggests that the strong variability observed for 3C 111 is probably driven by a change in the primary continuum.

**Key words:** galaxies: active – galaxies: radio – quasars: individual: 3C 111 – X-rays: galaxies

## 1 INTRODUCTION

The unified model of Active Galactic Nuclei (AGN) predicts that the ability of an accretion disk-black hole system to produce powerful relativistic jets is the main reason of the observed differences between radio loud (RL) and radio quiet (RQ) sources. Geometrical effects, through the relative inclination of an axisymmetric system with respect to the line of sight, can explain the majority of the differences between the various subclasses (Antonucci 1993; Urry & Padovani 1995). Although this model does work well to first order, it leaves still open a number of problems.

In particular, a key question still to be fully answered is why powerful relativistic jets are produced only in 10 – 20% of AGN, and if and how this is related to the structure of the accretion flow in the RL and RQ sources. In other

words, an often debated issue is how accretion and ejecta in AGN are linked, and how these mechanisms work under different physical conditions (e.g., Blandford & Znajek 1977; Blandford & Payne 1982; Sikora, Stawarz, & Lasota 2007; Garofalo 2009; Garofalo, Evans, & Sambruna 2010; Tchekhovskoy, Narayan, & McKinney 2010; for a parallel with X-ray binaries, see Fender, Gallo, & Russell 2010). A closely related question concerns the evolution of the jets, and its link with the observational subclasses of RL. It is commonly accepted that the relativistic jet originates in the innermost regions, and as the angle between the jet axis and the line of sight decreases, the importance of its emission increases, due to beaming effects. This simple picture does not account for the whole RL phenomenology, different global properties being associated to sources with different radio morphology (e.g., Hardcastle, Evans, & Croston 2007; Daly 2009a,b).

\* E-mail: ballo@ifca.unican.es (LB)

A key observational challenge in RL AGN is to disentangle

the jet contribution from the disk emission, which could allow us to better understand what are the main differences in the nuclear regions between RL and RQ sources. Previous X-ray observations of RQ and RL objects established that these sources exhibit spectra with subtle but significant differences (e.g., Zdziarski & Grandi 2001; Sambruna, Eracleous, & Mushotzky 2002). The X-ray emission of RQ objects appears to be described at first order by a primary power-law continuum, with features resulting from the reprocessing of this primary continuum from cold and warm gas, like the iron K line complex at 6 keV, the reflection component, and often ionized absorption and emission features. The main observed difference between RL and RQ sources is that the features due to reprocessing in RL AGN appear to be weaker compared to the RQ population (Ballantyne 2007, and references therein).

To account for these properties, several scenarios have been suggested. Highly ionized accretion disks, different from the standard, cold disk typical of Seyferts, could be obtained if the accretion rates are high (Ballantyne, Ross, & Fabian 2002). A difference in the inner accretion disks of BLRGs and RQs could result in a small solid angle subtended in RLs by the disk to the primary X-ray source (Eracleous, Sambruna, & Mushotzky 2000). On the other hand, assuming the same disk structure in both populations, dilution by non-thermal jet emission could weaken the reprocessing features (Grandi, Urry, & Maraschi 2002).

It is however important to notice that in the last few years XMM-Newton and Suzaku are changing this simplistic view: observations of large samples of RQ AGN are showing a large spread in the X-ray properties of this class, with a wider range of continuum slopes and with several cases of sources having little or no reflection. It is thus emerging that the distinction between the two classes is not so sharp, but rather that RL objects populate one end of the distribution for Seyferts and quasars (QSOs; Sambruna et al. 2009, and references therein).

Strong signatures of low- and high-velocity outflows are rather common in RQ (e.g., Turner & Miller 2009). Warm absorbers (outflowing with velocities  $v \sim 100 - 1000$  km/s) are detected in the soft X-ray spectra of more than half of local Seyfert galaxies (e.g., Crenshaw, Kraemer, & George 2003; Blustein et al. 2005). Their location at  $\sim 1 - 100$  pc suggests a possible association with the optical Broad Line Region (BLR) or Narrow Line Region. Ultra-fast outflows, showing velocities  $v > 10000$  km/s, have been found to be present in  $\sim 40\%$  of local Seyferts (Tombesi et al. 2010a). Their location on sub-pc scales suggests a direct association with accretion disk winds/outflows.

Regarding RL objects, only in the last few years have sensitive and broad-band observations started to detect disk winds/outflows in Broad Line Radio Galaxies (BLRGs). Chandra and XMM-Newton observations of 3C 382 revealed the presence of a warm absorber with outflow-like properties (Reeves et al. 2009; Torresi et al. 2010), while 3C 445 shows signatures of soft X-ray photoionized gas in emission and absorption (see Sambruna, Reeves, & Braitto 2007; Reeves et al. 2010; Braitto et al. 2011). Our Suzaku observations provided evidence for ultra-fast disk outflows in 3/5 BLRGs (blueshift velocity  $v_{\text{out}} \sim 0.04 - 0.15 c$ , and mass outflow rates comparable to the accretion rates; Tombesi et al. 2010b).

Differences in terms of the strength of the reflection features, as well as the presence or lack of warm absorbers or high-velocity outflows, in sources showing different radio properties is one of the natural consequences of the so-called “gap-paradigm” (Garofalo 2009; Garofalo, Evans, & Sambruna 2010). Its main ingredient is the relative orientation of the disk and the black hole spin; the abil-

ity of the source of producing powerful jets is related to retrograde systems. In particular, this model accounts for the weaker reflection features observed in BLRGs, a natural consequence of the larger gap between the innermost stable circular orbit of the disk and the black hole in retrograde sources than in prograde objects. At the same time, the model provides a simple interpretation for the presence or absence of signatures of disk winds, depending on the size of the gap region and the accretion efficiency.

An additional complication in the study of the properties of the accretion flow in RL and RQ, is the presence in the former of emission due to the jet, that can mask the thermal emission (directly observed and/or reprocessed) from the disk. From the observational point of view, only through a wide energy coverage and good sensitivity at medium-hard X-rays, can we attempt to disentangle the contribution of the jet and the disk emission. The request of both simultaneous broadband coverage and high sensitivity in the iron K line region has now been achieved with Suzaku. We then started a program aimed to observe with this satellite the brightest (and best studied) BLRGs. Here we present the X-ray view of the BLRG 3C 111 obtained thanks to our Suzaku data and an archival long exposure with XMM-Newton; Table 1 summarizes the main global properties of the source.

The paper is organized as follows. The main properties of the source and previous X-ray results are presented in Section 2. Sections 3 and 4 describe the X-ray observations and data analysis. Our results are discussed in Section 5, and finally in Section 6 we summarize our work. Throughout this paper, a concordance cosmology with  $H_0 = 71$  km s $^{-1}$  Mpc $^{-1}$ ,  $\Omega_\Lambda = 0.73$ , and  $\Omega_m = 0.27$  (Spergel et al. 2003, 2007) is adopted. The energy spectral index,  $\alpha$ , is defined such that  $F_\nu \propto \nu^{-\alpha}$ . The photon index is  $\Gamma = \alpha + 1$ .

## 2 THE BLRG 3C 111

3C 111 is a nearby ( $z = 0.0485$ ), well-studied BLRG with broad optical lines [FWHM(H $\alpha$ )  $\sim 4800$  km s $^{-1}$ ; Eracleous & Halpern 2003]. It exhibits a Fanaroff-Riley II radio morphology, with a single-sided jet (Linfield & Perley 1984) showing superluminal motion (Vermeulen & Cohen 1994). From the measured proper motion [ $\mu = (1.54 \pm 0.2)''$  yr $^{-1}$ ] and the maximum angular size of the radio lobes ( $\theta = 273''$ ; Nilsson et al. 1993), Lewis et al. (2005) inferred a range of  $10^\circ < i < 26^\circ$  ( $21^\circ < i < 26^\circ$  unless the source is a giant radio galaxy) for the inclination angle of the jet. A recent estimate of the jet inclination of  $i \sim 19^\circ$  has been derived with a Very Long Baseline Array (VLBA) monitoring (from the MOJAVE program; Kadler et al. 2008). This program revealed also the presence of a variety of components in the jet of 3C 111: a compact core, superluminal jet components, recollimation shocks, and regions of interaction between the jet and its surrounding medium.

From the relation with the bulge luminosity, Marchesini, Celotti, & Ferrarese (2004) estimated a black hole mass for 3C 111 of  $M_{\text{BH}} = 3.6 \times 10^9 M_\odot$ . New estimates, derived from measurements of the H $\alpha$  width (Chatterjee et al. 2011), range from  $1.5 \times 10^8 M_\odot$  to  $2.4 \times 10^8 M_\odot$ , more than a factor 10 lower than the values derived by Marchesini, Celotti, & Ferrarese (2004). As suggested by Chatterjee et al. (2011), this difference is probably due to the different extinction adopted in the two papers.

Several high-energy observatories targeted 3C 111. Simultaneous RXTE and XMM-Newton observations (Lewis et al. 2005) revealed a rather flat continuum ( $\Gamma \sim 1.63 - 1.75$ , depending on

**Table 1. Main global properties of 3C 111.**

RA (J2000)	Dec (J2000)	Redshift	$N_{\text{H, gal}}$ [ $10^{20} \text{ cm}^{-2}$ ]	FWHM[H $\alpha$ ] [ $\text{km s}^{-1}$ ]	$i$ [deg.]	$M_{\text{BH}}$ [ $10^8 M_{\odot}$ ]	$R_{\text{g}}$ [ $10^{14} \text{ cm}$ ]	$\log L_{\text{bol}}$ [ $\text{erg s}^{-1}$ ]	$\log L_{\text{bol}}/L_{\text{Edd}}$
(1)	(2)	(3)	(4)	(5)	(6)	(7)	(8)	(9)	(10)
04h18m21.3s	+38d01m36s	0.0485	29.1	4800	19	36.0	10.7	45.56	-2.11
					10 – 26	1.5 – 2.4	0.44 – 0.71	44.40 – 45.26	–
						1.8	0.53	44.68	-1.69

(1) Right Ascension. (2) Declination. (3) Cosmological redshift. (4) Neutral Galactic absorption column density (Kalberla et al. 2005). (5) Full Width Half Maximum of the optical line (Eracleous & Halpern 1994, 2003). (6) Inclination angle of the jet, from radio observations (Kadler et al. 2008; Eracleous, Sambruna, & Mushotzky 2000); in the second row, the range inferred by Lewis et al. (2005) is reported. (7) Black-hole mass: in the first row, from Marchesini, Celotti, & Ferrarese (2004); in the second row, the range recently proposed by Chatterjee et al. (2011), which intermediate value is reported in the third row. (8) Schwarzschild radius; in each row, the value inferred from the corresponding black hole mass. (9) Bolometric luminosity: in the first row, estimated by Marchesini, Celotti, & Ferrarese (2004) from the optical luminosity; in the second row, the range recently proposed by Chatterjee et al. (2011), which intermediate value is reported in the third row. (10) Eddington ratio, from the black hole mass and bolometric luminosity reported in columns (7) and (9), respectively.

the adopted model) and an extremely weak reflection component<sup>1</sup>,  $R \lesssim 0.3$ . To explain the broad residuals found in the iron K energy range, the authors assumed either reprocessed emission (i.e., reflection component and broad iron K emission line) from a truncated accretion disk, or a partial covering absorber with high column density ( $N_{\text{H}} \sim 10^{23} \text{ cm}^{-2}$ ); although the two parametrizations were not distinguishable from the fitting point of view, the latter model, though less complex, was disfavoured by the authors on physical grounds (mainly in view of the small inclination angle of the jet). Regardless of the continuum model used, a narrow Fe K $\alpha$  line arising in a distant reprocessor is required, with equivalent width (EW)  $\sim 20 - 30 \text{ eV}$ .

A *BeppoSAX* observation of 3C 111 confirmed that a flat continuum is present ( $\Gamma \sim 1.58$ ), with only upper limits for the reflection component and the Fe K $\alpha$  line (EW  $< 72 \text{ eV}$ ,  $R < 0.3$ ; Grandi, Malaguti, & Fionchi 2006). However, a re-analysis of the same *BeppoSAX* data presented in Dadina (2007) found a steeper continuum ( $\Gamma \sim 1.75$ ) and a higher upper limit for the reflection parameter,  $R \leq 2.25$ ; the *BeppoSAX* data provides only a lower limit to the high-energy cutoff,  $E_{\text{c}} \geq 82 \text{ keV}$ .

The 6-years of monitoring with *RXTE* recently presented in Chatterjee et al. (2011) highlights the long time-scale variability of 3C 111. The flux shows a range of variability  $F_{2-10\text{keV}} \sim 2 \times 10^{-11} - 8 \times 10^{-11} \text{ ergs cm}^{-2} \text{ s}^{-1}$  (i.e., a factor of  $\sim 4$ ), clearly correlated with the variation in the X-ray photon index. From their analysis of the variations in the X-ray continuum and Fe K $\alpha$  emission line, the authors conclude that the iron line is generated within 90 light-days of the source of the X-ray continuum. The latter can be either the corona or the base of the jet; in both cases, the *RXTE* data are consistent with the standard paradigm of X-ray emission dominated by reprocessing of thermal photons produced in the accretion disk; no strong contribution from the jet is observed.

A 10 ks *Chandra* exposure detected an excess of X-ray emission in 3 radio knots out of the 4 present along the single sided jet structure, as well as in its terminal point (Hogan et al. 2011). The emission is ascribed by the authors to inverse Compton scattering off of cosmic microwave background photons (IC/CMB). Thus, depending on the adopted model for the jet structure from pc to kpc scales (e.g., jet bending and/or deceleration, or neither of them), the

combined *Chandra* and VLBI observations imply for the kpc-scale jet bulk Lorentz factor a range between  $\sim 3.5$  and  $7.2$ .

In the  $\gamma$ -ray band, a  $3\sigma$  *Egret* detection was reported for this source (Sguera et al. 2005; Hartman, Kadler, & Tueller 2008), as well as an association with a *Fermi* source (Abdo et al. 2010), implying a broad-band SED reminiscent of a de-beamed blazar. Comparing  $\gamma$ -ray and multiwavelength properties for a sample of *Fermi*-detected and *Fermi*-undetected BLRGs, Kataoka et al. (2011) suggest that the GeV emission from 3C 111 is most likely dominated by the beamed radiation from the nuclear region of the relativistic jet.

### 3 X-RAY OBSERVATIONS

#### 3.1 *Suzaku*

*Suzaku* observed 3C 111 at the HXD (Hard X-ray Detector, Takahashi et al. 2007) nominal pointing position on 22 of August, 2008 for a total exposure time of about 122 ks. The log of the X-ray observations is reported in Table 2, first part. We used the cleaned event files obtained from version 2 of the *Suzaku* pipeline processing. Standard screening criteria were used, namely, only events outside the South Atlantic Anomaly (SAA) as well as with an Earth elevation angle (ELV)  $> 5^\circ$  were retained, and Earth day-time elevation angles (DYE\_ELV)  $> 20^\circ$ . Furthermore, data within 256 s of the SAA passage were excluded and a cut-off rigidity of  $> 6 \text{ GV}$  was adopted.

XIS (X-ray Imaging Spectrometer, Koyama et al. 2007) data were selected in  $3 \times 3$  and  $5 \times 5$  editmodes using grades 0, 2, 3, 4, 6, and cleaned for hot and flickering pixels. The XIS spectra of 3C 111 were extracted from circular regions centred on the sources of  $2.9'$  radius. Background spectra were extracted from two regions, each with the same area of the main target region, offset from the main target and avoiding the calibration sources. The XIS response and ancillary response files were produced, using the latest calibration files available, with the *ftools* tasks *xisrmfgen* and *xissimarfgen*, respectively.

We tested time-variability within the *Suzaku* observation, generating source light curves in the soft and hard energy ranges with a binning time of 5760 sec, the orbital period of the satellite, to remove any possible modulation related to the orbital condition. Fig. 1 shows the soft and hard X-ray light curves obtained with the XISs, and their hardness ratios. The data from XIS0, XIS3, and

<sup>1</sup> The reflection fraction  $R$  is defined as  $R = \Omega/2\pi$ , where  $\Omega$  is the solid angle subtended by the Compton-thick matter to the X-ray source; for a plane parallel slab,  $R = 1$ .

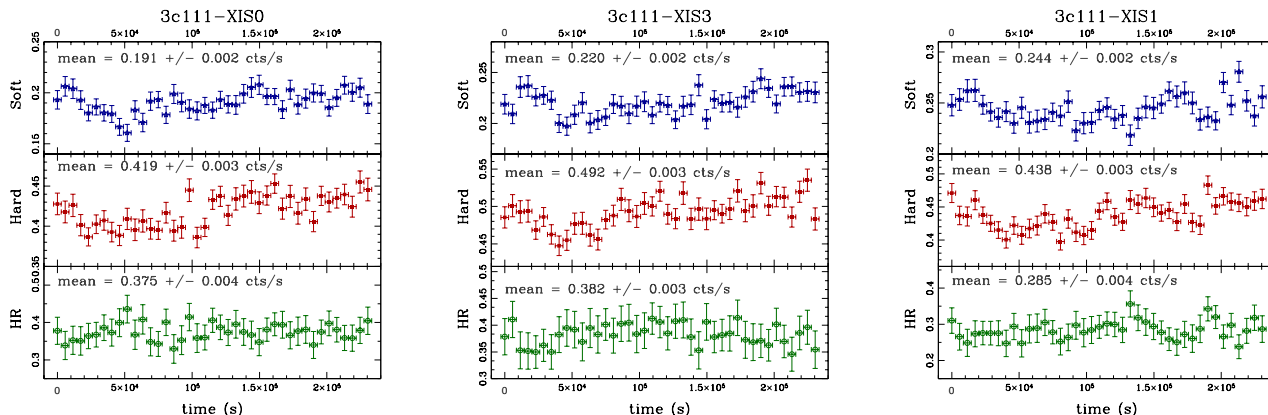


**Figure 1.** Background-subtracted light curves of 3C 111 from the *Suzaku* XIS0 (left panels), XIS3 (middle panels), and XIS1 (right panels) observations, with a 5760 sec bin. *Upper panels:* 0.5 – 2 keV; *middle panels:* 2 – 10 keV; *lower panels:*  $HR = [RATE_{2-10} - RATE_{0.5-2}] / [RATE_{2-10} + RATE_{0.5-2}]$ . In each panel, we report the mean rate [HR] for the whole observation.

XIS1 are plotted on separate panels, from *left to right*. The source displays a hint of variability, with the  $\chi^2$  probability of constancy less than 30% and 5% in the soft and hard band, respectively. However, the HR light curves show a lack of significant spectral variability. Therefore, in the following spectral analysis we considered the time-averaged data over the whole duration of the observation.

After checking that the spectra were consistent, we coadded the two front illuminated (FI) CCD spectra<sup>2</sup>, along with the response files, to maximize the signal-to-noise ratio. The FI spectrum was then fitted jointly with the back illuminated (BI, the XIS1) spectrum.

The net FI [BI] source spectra were rebinned to 1024 channels and then grouped with a minimum of 200 [100] counts per bin. Data were included from 0.6 to 10 keV [8.5 keV], observed frame; the region around the Si K edge between 1.7 and 1.9 keV were discarded in both the FI and BI XIS, due to uncertainties in the calibration at this energy. The net background-subtracted source count rates for 3C 111 were  $0.609 \pm 0.002$ ,  $0.712 \pm 0.003$  and  $0.676 \pm 0.003$  counts  $s^{-1}$  for XIS0, XIS3 and XIS1 respectively, with a net exposure time after screening of 109 ks.

For the HXD-PIN data reduction and analysis we followed the *Suzaku* data reduction guide (the ABC guide<sup>3</sup> Version 2). We used the rev2 data, which include all four cluster units, and the best background available, which account for non-X-ray background (NXB<sup>4</sup>; Kokubun et al. 2007).

At the time of this analysis, two NXB files are available: background A or “quick” background and background D or “tuned” background. We adopted the latter, which is the latest release and which suffers lower systematic uncertainties of about 1.3%, corresponding to about half uncertainty of the first release of the NXB. We confirmed this choice as most reliable estimate of the NXB by comparing the background A or D light curve to the light curve obtained from the Earth occulted data (from Earth elevation angles  $ELV < -5$ ): indeed, the Earth occulted data give a representation

of the actual NXB rate, as this neither includes a contribution from the source nor from the cosmic X-ray background.

The source and background spectra were extracted within the common good time interval and the source spectrum was corrected for the detector deadtime. The contribution of the diffuse cosmic X-ray background counts was simulated using the spectral form of Boldt (1987), assuming the response matrix for diffuse emission, and then added to the NXB. With this choice of background, 3C 111 is detected up to 70 keV at a level of 19% above the background. The net exposure time after screening was 102 ks. The HXD-PIN spectrum was binned in order to have a signal-to-noise ratio greater than 10 in each bin, and the latest response file released by the instrumental team was used. The count rate in 14 – 70 keV is  $0.081 \pm 0.002$  counts  $s^{-1}$ . Assuming a single cutoff power-law component ( $\Gamma \sim 1.6$  and  $E_c \sim 100$  keV) this corresponds to a  $F_{14-70\text{keV}} \sim 4 \times 10^{-11}$  ergs  $cm^{-2} s^{-1}$ . In the spectral analysis, we used a cross-calibration constant of 1.18 between the HXD and XIS spectra, as suggested by the *Suzaku*-HXD calibration team for observation at the HXD nominal pointing position<sup>5</sup>.

Following the prescription<sup>6</sup>, we reprocessed the GSO data from the unscreened events, using the new gain calibration as of August 2010, in order to apply the correct GSO gain history file. Note that using the new GSO background instead of the one with the old gain calibration implies a loss of time of  $\sim 33\%$ . As for the PIN, the GSO/NXB files was used in conjunction with the screened source events file to create a common good time interval. The cosmic X-ray background, not included in the background event files, can be neglected, being less than 0.1% of the total background rate in the GSO. Both source and background spectra were corrected for the detector deadtime, and the former was rebinned for the background subtraction, because the GSO background is created in 64 bins.

3C 111 is marginally detected with the HXD/GSO. The background-subtracted GSO count rate in the 50 – 200 keV band is  $0.06 \pm 0.03$  counts  $s^{-1}$ , corresponding to a  $S/N \sim 1.3$  (0.3% of the total), for a net exposure time of 68 ks.

<sup>2</sup> XIS0 and XIS3, found to be consistent within 5% cross-normalization uncertainties

<sup>3</sup> <http://heasarc.gsfc.nasa.gov/docs/suzaku/analysis/abc/>

<sup>4</sup> <ftp://legacy.gsfc.nasa.gov/suzaku/doc/hxd/suzakumemo-2008-03.pdf>

<sup>5</sup> <http://heasarc.nasa.gov/docs/suzaku/analysis/watchout.html>

<sup>6</sup> [http://heasarc.gsfc.nasa.gov/docs/suzaku/analysis/hxd\\_repro.html](http://heasarc.gsfc.nasa.gov/docs/suzaku/analysis/hxd_repro.html)

Table 2. Observation log.

Satellite	Sequence N.	Start (U.T.)	Stop (U.T.)	Detector	Exposure [ks]	Count Rate [counts/s]		
(1)	(2)	(3)	(4)	(5)	(6)	(7)		
<i>Suzaku</i>	703034010	2008-08-22 09:37:00	2008-08-25 04:24:00	XIS0	108.9	0.609 ± 0.002		
				XIS3	108.9	0.712 ± 0.003		
				XIS1	108.9	0.676 ± 0.003		
				PIN	101.9	0.081 ± 0.002		
				GSO	68.1	0.060 ± 0.023		
<i>XMM-Newton</i>	0552180101	2009-02-15 19:41:57	2009-02-17 04:00:49	pn	59.1	5.113 ± 0.009		
				MOS2	60.9	2.046 ± 0.006		
				RGS1	83.3	0.086 ± 0.001		
<i>XMM-Newton</i>	0065940101	2009-02-15 18:59:02	2009-02-17 04:10:44	RGS2	83.2	0.106 ± 0.001		
				2001-03-14 12:56:20	2001-03-15 01:20:36	RGS1	32.3	0.132 ± 0.002
						RGS2	31.5	0.162 ± 0.002

(1) X-ray satellite. (2) Sequence number of the observation. (3) Starting date (in year-month-day) and time (in hh:mm:ss) of the observation. (4) End date (in year-month-day) and time (in hh:mm:ss) of the observation. (5) Detector on-board the satellite. (6) Exposure time after screening was applied to the data. (7) Net source count rate after screening and background subtraction, as observed in the 0.6 – 10 keV (XIS0 and XIS3), 0.6 – 8.5 keV (XIS1), 14 – 70 keV (PIN), 50 – 200 keV (GSO), 1 – 10 keV (pn, pattern 0), 0.4 – 10 keV (MOS2, pattern 0), and 0.65 – 2 keV (RGS) energy ranges.

### 3.2 XMM-Newton

XMM-Newton observed 3C 111 twice, in March 2001 for about a total of 45 ksec (Obs. ID 0065940101), and in February 2009 for about a total of 120 ks (Obs. ID 0552180101). The analysis of the former observation is presented in Lewis et al. (2005); the pn 2.4 – 10 keV light curve from the second observation is included in the X-ray monitoring presented by Chatterjee et al. (2011, their “longlook data”). Here we present the analysis of the still unpublished X-ray spectra obtained in the second pointing.

The observations were performed with the European Photon Imaging Camera (EPIC), the Optical Monitor (OM) and the Reflection Grating Spectrometer (RGS). The observation details are reported in Table 2, second part. In this paper, we concentrate on the data in the X-ray band.

The three EPIC cameras (pn, MOS1, and MOS2; Strüder et al. 2001; Turner et al. 2001) were operating in Small Window mode, with the thin filter applied. The XMM-Newton data have been processed, and event lists for the EPIC cameras were produced, using the Science Analysis Software (SAS version 10.0.2) with the most recent calibrations.

EPIC event files have been filtered for high-background time intervals, following the standard method consisting in rejecting periods of high count rate at energies > 10 keV. Given the X-ray brightness of the source, to avoid pile-up effects only events corresponding to pattern 0 have been used (see the XMM-Newton Users’ Handbook; Ness et al. 2010). We have also generated the spectral response matrices at the source position using the SAS tasks *arfgen* and *rmfgen*.

Source counts were extracted from a circular region of radius 25” and 30” for the MOS2 and pn cameras, respectively. For the pn camera, background counts were extracted from two source-free circular regions in the same chip of 50” radius each. Background counts for MOS2 were extracted from similar regions but selected outside the central chip, symmetric with respect to the source position. Regarding the MOS1, in addition to two bad pixel columns near the source, a careful look to the images extracted in RAWX,RAWY coordinates revealed the presence of two more dark columns falling in the centre of the source, not visible using x,y coordinates, strongly affecting the spectral shape. Therefore, we

decided to not use the data from the MOS1 camera, limiting the analysis of XMM-Newton only to the MOS2 and pn spectra.

According to the result of the SAS task *epatplot* applied to the cleaned event file, pn data are affected by “X-ray loading”, i.e. the inclusion of X-ray events in the offset map calculation<sup>7</sup>. This phenomenon, observed in very bright sources, is a consequence of excessive count rate, and occurs at lower source count rate than the pile-up threshold. The effects are a systematic energy shift to low energy and pattern migration from doubles to single events. As the pn offset maps are calculated on-board at the start of each exposure, for this camera the effects are hard to be reduced, therefore the pn data are more easily prone to this problem than the MOS one. At present, a reliable method to correct for this effect is not available. We then decided to discard the pn data in the soft energy range, more affected by the problem. The spectral shape of the pn spectrum above 1 keV is consistent with the MOS2 one, and with the *Suzaku* spectrum; this confirms that the selected band is not affected by the X-ray loading problem. Therefore, during the analysis we considered the energy range between 0.4 [1] and 10 keV for the MOS2 and the pn, respectively.

As previously performed for *Suzaku*, we checked pn and MOS2 data for variability during the observation using the SAS task *lcplot*. No bin shows significant deviation from the mean value, allowing us to perform the spectral analysis over the time-averaged spectra. Both pn and MOS2 spectra were grouped to have at least 200 counts in each energy bin.

The RGS (den Herder et al. 2001) data have been reduced using the standard SAS task *rgsproc*, and the most recent calibration files; after filtering out the high-background time intervals, the total exposure times are ~ 83 ks for both RGS1 and RGS2. The RGS1 and RGS2 spectra were binned at twice the instrument resolution,  $\Delta\lambda = 0.2 \text{ \AA}$ .

### 3.3 Swift BAT

The averaged BAT spectrum of this radiogalaxy was obtained from the 58-month survey archive (SWIFT J0418.3 + 3800). The data reduction and extraction procedure of the 8-channel spectrum is

<sup>7</sup> <http://xmm2.esac.esa.int/docs/documents/CAL-TN-0050-1-0.ps.gz>

described in Baumgartner et al. (2010). To fit the preprocessed, background-subtracted BAT spectra, we used the latest calibration response `diagonal_rsp` as of December 2010.

3C 111 was detected in the 15–100 keV band with a count rate  $(1.02 \pm 0.03) \times 10^{-3}$  counts  $s^{-1}$ , which correspond to a 14–195 keV flux of  $1.2 \pm 0.1 \times 10^{-10}$  ergs  $cm^{-2}$   $s^{-1}$  (Baumgartner et al. 2010).

Fitting the averaged BAT spectrum with the HXD best-fit model ( $\Gamma \sim 1.6$  and  $E_c \sim 100$  keV), we found  $F_{14-70\text{keV}}^{\text{BAT}} \sim 7 \times 10^{-11}$  ergs  $cm^{-2}$   $s^{-1}$ , while  $F_{14-70\text{keV}}^{\text{PIN}} \sim 4 \times 10^{-11}$  ergs  $cm^{-2}$   $s^{-1}$  (see Table 3). The comparison between the BAT and the PIN spectra suggests a possible hard X-ray variability on longer timescales: fitting the two spectra together and allowing to vary the relative normalizations, we found that we need the cross-normalization between the two instruments to be  $\sim 1.6$ , well above the uncertainties in the relative normalizations. The 58-month BAT lightcurve<sup>8</sup>, provided with the catalogue, suggests the presence of hard X-ray variability and that the *Suzaku* observation took place during an upswing after reaching a minimum of the 14–195 keV flux. We caution that the *Swift* spectrum used here is the averaged spectrum.

#### 4 X-RAY SPECTRAL ANALYSIS

All spectral fits to the X-ray data were performed using XSPEC v.12.6.0q. The significance of adding free parameters to the model was evaluated with the F-test, with associated probability  $P_F$ <sup>9</sup>. All uncertainties are quoted at the 90% confidence level for one parameter of interest ( $\Delta\chi^2 = 2.71$ ). Unless otherwise stated, the figures are in the rest-frame of 3C 111, and fit parameters are quoted in the same frame. All the models discussed in the following assume Galactic absorption with a column density of  $N_{\text{H,Gal}} \sim 2.91 \times 10^{21}$   $cm^{-2}$  (see Table 1; Kalberla et al. 2005). It is worth noting that for 3C 111 the estimate of the total Galactic hydrogen column density is not trivial: due to the presence of a dense molecular cloud along the line of sight, its value can be as high as  $N_{\text{H,Gal}} \sim 1.3 \times 10^{22}$   $cm^{-2}$  (Lewis et al. 2005, and references therein), and it is expected to vary by several times  $10^{21}$   $cm^{-2}$ . Therefore we allowed the local absorption to vary up to  $1.3 \times 10^{22}$   $cm^{-2}$ ; for this absorber we used the `phabs` model in XSPEC, adopting cross-sections and abundances of Wilms, Allen, & McCray (2000).

##### 4.1 *Suzaku*

The medium-energy spectrum of 3C 111 confirms the presence of strong iron K emission detected in previous observations (Lewis et al. 2005; Grandi, Malaguti, & Fiocchi 2006; Dadina 2007). We first fitted the XIS and PIN data (between 0.6 and 70 keV) with a single absorbed power-law component, excluding the energy range where the iron K complex is expected (5–8 keV). After including the 5–8 keV data, this model clearly provides a poor fit [ $\chi^2/\text{d.o.f.} = 1046.70/743$ ;  $\Gamma = 1.61 \pm 0.01$  and  $N_{\text{H}} = (1.20 \pm 0.02) \times 10^{22}$   $cm^{-2}$ ]; furthermore, large-amplitude residuals are present both in emission and in absorption (see Fig. 2). No additional intrinsic  $N_{\text{H}}$  is required ( $\Delta\chi^2/\Delta\text{d.o.f.} = 0.06/1$ ); however, taking into account the strong variability of  $N_{\text{H,Gal}}$  for 3C 111, we cannot exclude that some of the observed absorption is at the source redshift.

<sup>8</sup> [http://swift.gsfc.nasa.gov/docs/swift/results/bs58mon/mosaic\\_crab\\_lc/BAT\\_58m\\_crabweighted\\_monthly\\_SWIFT\\_J0418.3+3800.lc.gz](http://swift.gsfc.nasa.gov/docs/swift/results/bs58mon/mosaic_crab_lc/BAT_58m_crabweighted_monthly_SWIFT_J0418.3+3800.lc.gz)

<sup>9</sup> But see the caveats in using the F-test to measure the significance of narrow lines described in Protassov et al. (2002).

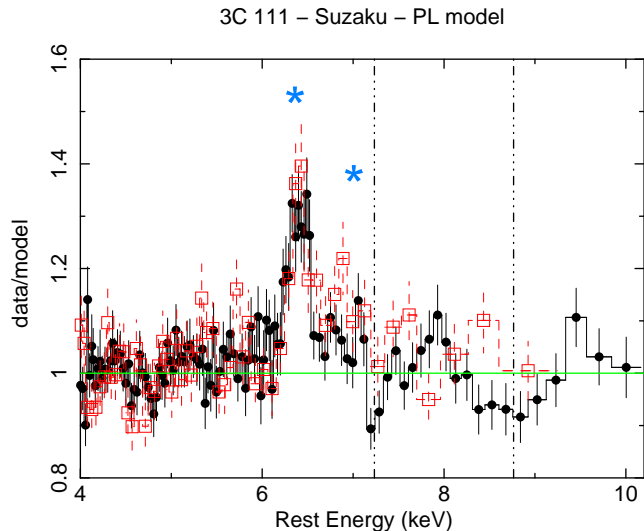


**Figure 2.** Data-to-model ratio for the *Suzaku* spectra (red open squares, XIS1; black filled circles and line, FI XIS). The model is an absorbed power-law component ( $\Gamma \sim 1.61$ ) fitted ignoring the 5–7.5 keV energy band, where the iron K complex is expected. For graphical purposes, the data have been binned to have a significance of  $17\sigma$ . The positions of the iron K lines (Fe  $K\alpha$  at 6.4 keV and Fe  $K\beta$  at 7.06 keV rest frame) are marked with a blue star. The vertical lines represent the centroids of the detected absorption lines in the FI XIS data (see Tombesi et al. 2010b).

The addition of a Gaussian line to the simple absorbed power-law component results in a large improvement in the fit ( $\Delta\chi^2/\Delta\text{d.o.f.} = 244.5/3$ ). The profile of the Fe  $K\alpha$  line ( $E = 6.40 \pm 0.02$  keV,  $\sigma = 94_{-22}^{+31}$  eV;  $F = 2.36_{-0.26}^{+0.46} \times 10^{-5}$  photons  $cm^{-2}$   $s^{-1}$ ,  $\text{EW} = 94_{-18}^{+13}$  eV) is marginally resolved, suggesting a possible contribution from the external disk and/or the BLR. However, constraining the iron K line to be narrow (10 eV) does not leave strong residuals which could be due to an additional broad component. The strength of the Fe  $K\alpha$  line, coupled with the hard photon index ( $1.59 \pm 0.01$ ) could suggest the presence of a reflection component. However, adding a reflection component (parametrized using the `pexrav` model in XSPEC; Magdziarz & Zdziarski 1995) to the absorbed cutoff power law plus iron line, we obtained a weak reflection fraction,  $R = 0.16_{-0.09}^{+0.11}$  ( $\chi^2/\text{d.o.f.} = 782.7/738$ ). During the fit, the abundance was fixed to the Solar one; the photon indices of the cutoff power law and the reflection component, as well as their energy cutoff, were set to be equal. Allowing the high energy cutoff to vary we can set only a lower limit ( $E_c > 75$  keV). The inclination angle (allowed to vary between  $10^\circ$  and  $26^\circ$ ; Lewis et al. 2005), is also not constrained by the present data. We therefore decided to fix both parameters (see below).

Although the energy centroid of the Fe  $K\alpha$  line suggests a low ionization reflector, we tested for a possible ionized reflector. We used an updated model for the Compton reflection off an optically thick photoionized slab of gas, which includes the iron K emission line (`reflionx` model in XSPEC; Ross, Fabian, & Young 1999; Ross & Fabian 2005); as expected the ionization of the reflector is found to be low,  $\xi < 13.9$  erg  $cm^{-2}$   $s^{-1}$ , being the ionization parameter mainly driven by the energy centroid of the Fe  $K\alpha$  line.

As the reflection component is weak and poorly constrained, we bounded its normalization to that of the emission line: to fit the two components in a consistent way, the ratio of their normal-

**Table 3. X-ray fluxes and luminosities.**

Satellite	Flux <sup>a</sup>		
	[10 <sup>-12</sup> ergs cm <sup>-2</sup> s <sup>-1</sup> ]		
	0.5 – 2 keV	2 – 10 keV	14 – 70 keV
<i>Suzaku</i>	2.55 <sup>+0.05</sup> <sub>-0.06</sub>	19.70 <sup>+0.52</sup> <sub>-0.48</sub>	40.21 <sup>+1.99</sup> <sub>-1.91</sub>
<i>XMM-Newton</i>	6.83 <sup>+0.07</sup> <sub>-0.11</sub>	48.32 <sup>+1.10</sup> <sub>-0.87</sub>	–
<i>Swift</i>	–	–	71.19 ± 2.45
Satellite	Luminosity <sup>b</sup>		
	[10 <sup>43</sup> ergs s <sup>-1</sup> ]		
	0.5 – 2 keV	2 – 10 keV	14 – 70 keV
<i>Suzaku</i>	5.44 <sup>+0.16</sup> <sub>-0.15</sub>	11.03 <sup>+0.28</sup> <sub>-0.27</sub>	21.69 <sup>+1.07</sup> <sub>-1.03</sub>
<i>XMM-Newton</i>	12.82 <sup>+0.23</sup> <sub>-0.11</sub>	27.54 <sup>+0.62</sup> <sub>-0.48</sub>	–
<i>Swift</i>	–	–	39.35 ± 1.36

Errors are quoted at the 90% confidence level for 1 parameter of interest ( $\Delta\chi^2 = 2.71$ ). <sup>a</sup> Observed fluxes. <sup>b</sup> Intrinsic luminosities, corrected for local absorption, as well as for the effects of the photoionized gas.

izations was assumed to be the expected one<sup>10</sup> for a face-on slab illuminated by a flat continuum ( $\Gamma \sim 1.6$ ), i.e.  $N_{\text{gauss}}/N_{\text{pexrav}} \sim 1.2 \times 10^{-2}$  (George & Fabian 1991; Nandra & George 1994; Matt, Fabian, & Ross 1996; Matt, Fabian, & Reynolds 1997). The  $R$  parameter was fixed to 1, the inclination angle to  $19^\circ$  (Kadler et al. 2008), and the energy cutoff of the primary power law and of the reflection component to 100 keV, a value consistent with the lower limit previously found. Higher values of  $E_c$  imply a slight decrease in the quality of the fit. We also included a neutral Fe K $\beta$  line (at an energy fixed to 7.06 keV) with a flux of 13.5% of the Fe K $\alpha$  line (Palmeri et al. 2003; Yaqoob et al. 2010) and the same width.

The baseline model then consists of: a rather flat cutoff power law ( $\Gamma = 1.61 \pm 0.01$ ), and a reflection continuum+two narrow iron K lines. The width of the line, allowed to vary during the fit, is  $\sigma = 70^{+27}_{-28}$  eV. The strength of the reflection, estimated as the ratio of the pexrav and the direct power-law normalizations, is  $N_{\text{pexrav}}/N_{\text{cutoffpl}} = 0.35 \pm 0.06$ . The column density is  $N_{\text{H}} = (1.20 \pm 0.02) \times 10^{22}$  cm<sup>-2</sup>. This model provides an acceptable description for the broadband X-ray spectrum of 3C 111 ( $\chi^2/\text{d.o.f.} = 793.8/740$ ).

However, some residuals suggest the presence of lines in emission, around 0.9 keV, and in absorption, between 6 and 9 keV (see Fig. 3 and Fig. 4). To account for this residuals we first added to the baseline model 3 Gaussian lines (2 absorption and one emission lines). Including a narrow emission Gaussian component ( $\sigma$  fixed to 10 eV) at low energies, the improvement in the fit is significant ( $\Delta\chi^2/\Delta\text{d.o.f.} = 10.2/2$ , considering only 736 XIS bins between 0.6 and 10 keV); the energy is  $E = 0.89 \pm 0.01$  keV, with  $\text{EW} = 32^{+15}_{-10}$  eV. Tentatively, the line can be identified with the O VIII RRC or the Ne IX triplet lines. The two absorption lines are detected at the rest-frame energies of  $E = 7.23^{+0.06}_{-0.07}$  keV ( $\sigma$  fixed to 50 eV;  $\text{EW} = -15.2^{+10.8}_{-9.9}$  eV) and  $E = 8.76 \pm 0.20$  keV ( $\text{EW} = -48.9^{+28.5}_{-36.2}$  eV), with a  $\Delta\chi^2/\Delta\text{d.o.f.} = 9.5/2$  and  $10.9/3$ , respectively. We refer to the Monte Carlo simulations presented in Tombesi et al. (2010b) for a more robust estimate of the significance of the high-energy absorption lines in this *Suzaku* observation of 3C 111. We note that in their analysis the authors considered only the FI data, and adopted for the 3.5 – 10.5 keV continuum a single power law, resulting in a flatter photon index  $\Gamma \sim 1.47$  and a higher continuum model above  $\sim 7$  keV. However, given the lim-

3C 111 – Suzaku data – Baseline model

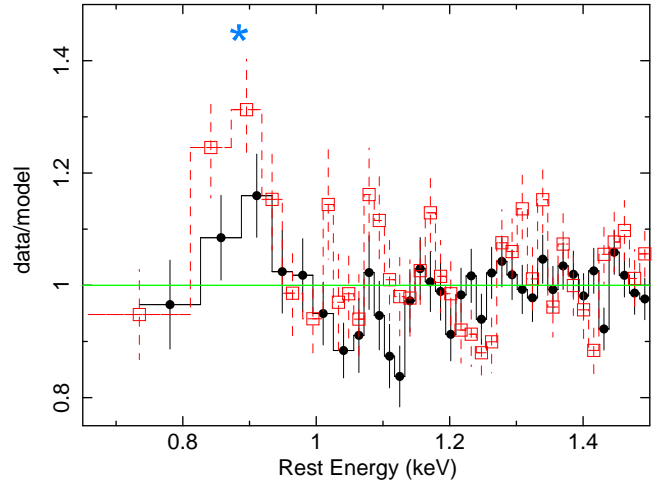


**Figure 3.** Data-to-model ratio for the *Suzaku* spectra below 1.5 keV; red open squares, XIS1; black filled circles and line, FI XIS. For graphical purposes, the data have been binned to have a significance of  $10\sigma$ . The adopted model is the baseline model (an absorbed cutoff power law and a reflection component, with superimposed two narrow Gaussian lines, the Fe K $\alpha$  at 6.4 keV and the Fe K $\beta$  at 7.06 keV rest frame). The centroid of the emission line when one more Gaussian is included in the model is marked with a blue star (emission line at  $E \sim 0.89$  keV).

3C 111 – Suzaku data – Baseline model

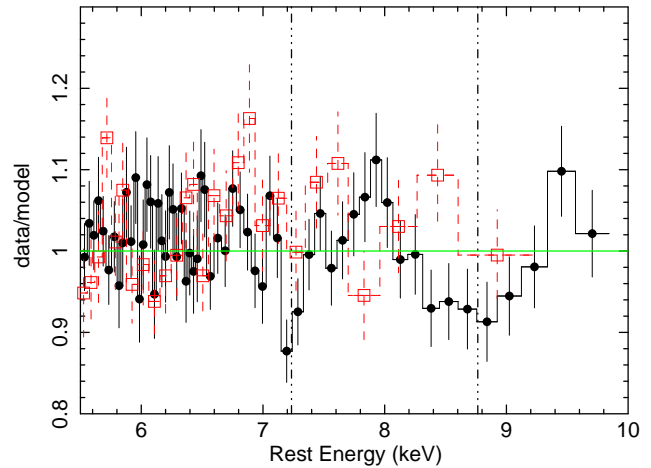


**Figure 4.** Data-to-model ratio for the *Suzaku* spectra above 5.5 keV; red open squares, XIS1; black filled circles and line, FI XIS. For graphical purposes, the data have been binned to have a significance of  $17\sigma$ . The adopted model is the baseline model (an absorbed cutoff power law and a reflection component, with superimposed two narrow Gaussian lines, the Fe K $\alpha$  at 6.4 keV and the Fe K $\beta$  at 7.06 keV rest frame). The centroids of the absorption lines when two more Gaussians are included in the model are marked with two vertical lines (absorption line at  $E \sim 7.2$  keV and  $E \sim 8.8$  keV).

ited energy band considered, the effect of this continuum model does not strongly affect the detection significance of the absorption lines. If we consider only FI data, as the XIS1 is less reliable in the iron K energy range, the significance of the absorption lines is:  $\Delta\chi^2/\Delta\text{d.o.f.} = 15.5/2$  and  $15.5/3$  for the line at  $E \sim 7.23$  keV and  $E \sim 8.76$  keV, respectively.

A detailed study of the absorption features and their interpre-

<sup>10</sup> <http://www.jca.umbc.edu/~george/html/science/seyferts/fgfplus.html>

tation in terms of ultra-fast outflows related with the accretion disk is reported in Tombesi et al. (2010b). Briefly, the most plausible association for the first absorption line is the resonant Fe xxvi Ly $\alpha$  transition at 6.97 keV. If the line is identified with this atomic transition, we have to assume a velocity shifts of  $v_{\text{out}} \sim -0.04 c$ . Concerning the second feature, it is likely a blend of different lines of the Fe xxvi Lyman series (namely, Ly $\beta$ , Ly $\gamma$ , and Ly $\delta$ ). In a more physically consistent modelling of the absorption feature, the absorber is parametrized using a grid of photoionized absorbers generated by the XSTAR<sup>11</sup> photoionization code (Kallman & Bautista 2001; Kallman et al. 2004). The photoionized gas is assumed to be fully covering the X-ray source with turbulence velocity  $v_{\text{turb}} = 500 \text{ km s}^{-1}$ , and illuminated by a power-law continuum from 0.0136 to 13.6 keV with photon index  $\Gamma = 2$ . It is important to note that a single photoionized absorber can account for both lines. The results of the fit are: high ionization state,  $\log \xi = 5.3^{+0.6}_{-1.2} \text{ erg cm s}^{-1}$ , with  $N_{\text{H}}^{\text{ion}} \sim 6.97 \times 10^{23} \text{ cm}^{-2}$  ( $N_{\text{H}}^{\text{ion}} > 1.45 \times 10^{22} \text{ cm}^{-2}$  at the 90% level), and blueshift velocity  $v_{\text{out}} = 0.038 \pm 0.006 c$  ( $\chi^2 = 768.2$  for 735 degree of freedom). We note that the high ionization state implied by  $\log \xi \sim 5.3 \text{ erg cm s}^{-1}$  does not introduce a significant curvature in the primary continuum below  $\sim 6 \text{ keV}$ . The outflow velocity is somewhat similar to the source cosmological redshift,  $z = 0.0485$ , and thus could suggest a contamination due to local or intermediate redshift absorbers (e.g., McKernan et al. 2003; McKernan, Yaqoob, & Reynolds 2004, 2005). However, this scenario is ruled out by the high column density implied for this absorber. We refer the reader to the discussion in Tombesi et al. (2010b, sect. 5.1), where the authors investigate in details this possibility and conclude that it is not feasible. The addition of the photoionized absorber improves the fit of  $\Delta\chi^2/\Delta\text{d.o.f.} = 13.8/3$ .

Observed fluxes and intrinsic luminosities are summarized in Table 3; the unfolded best fit to the data is shown in Fig. 5 (*upper panel*). The best-fit parameters are reported in the first part of Table 4; note that the inclusion of the warm absorber does not change significantly the continuum photon index or the emission lines parameters.

As a final test, taking into account the low reflection component and the flat continuum observed, we checked the presence of a second continuum emission due to the jet. To this end, we considered also the GSO detection of 3C 111, that extends the source spectral energy distribution (SED) up to  $\sim 200 \text{ keV}$ . Adding to the best fit model a second power law, with a flatter photon index ( $\Gamma_{\text{jet}} = 1.51 \pm 0.03$ ), we obtained for the primary cutoff power law a photon index in better agreement with values expected from disk emission,  $\Gamma = 1.70^{+0.06}_{-0.02}$ . We fixed the parameters of the lines, as well as the column density, the ionization state, and the velocity of the outflow, to the best-fit values previously found. This model provides a good description of the broadband X-ray spectrum of 3C 111,  $\chi^2/\text{d.o.f.} = 846.6/768$  (see Fig. 5, *bottom panel*). Despite the inclusion of the GSO data, the improvement in the fit due to the addition of this component is only  $\Delta\chi^2/\Delta\text{d.o.f.} = 3.1/2$  (F-test probability  $P_{\text{F}} = 75.6\%$ ). We note that the jet dominates only above 10 keV, thus the possibility to accommodate a jet component in the best-fit model is strongly related to the inclusion of the GSO detection in the fit. Moreover, the relative normalizations of the two power laws are degenerate, making it difficult to spectrally distinguish the true jet component.

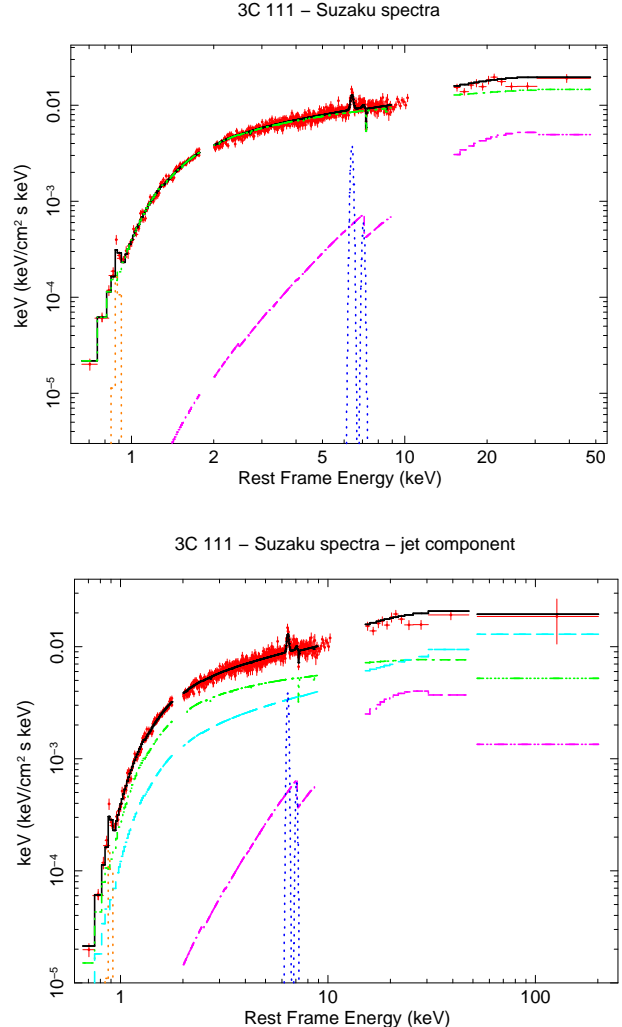


**Figure 5.** *Suzaku* XIS and HXD spectra of 3C 111, binned to have a significance of  $3\sigma$ . In both panels, the black lines represent the total best-fit model; the underlying continuum is modelled with a cutoff power-law component (green dash-dot-dotted lines) plus a weak reflection component (magenta dash-dotted lines). The iron K line complex is composed by a Fe K $\alpha$  and a Fe K $\beta$  features (blue dotted lines). In addition, an X-ray emission line at  $\sim 0.9 \text{ keV}$  is also shown (orange dotted lines). In the *bottom panel* we show the model when a component due to the jet is considered (light blue line); also reported is the detection in the GSO, extending the spectrum up to 200 keV.

## 4.2 XMM-Newton

The 0.6 – 10 keV XMM-Newton emission shape of 3C 111 is in good agreement with the best fit for the broad band continuum of *Suzaku*, both in the broad-band slope ( $\Gamma \sim 1.60$ ,  $N_{\text{H}} \sim 1.04 \times 10^{22} \text{ cm}^{-2}$ ) and in the detection of a strong Fe K $\alpha$  emission line (see Fig. 6). The main difference is in the observed flux, a factor  $\sim 2.5$  higher than the *Suzaku* flux, see Table 3. This is not surprising when the *RXTE* long-term light curve is considered (see fig. 1 in Chatterjee et al. 2011): the *Suzaku* observation took place during a recovery of the emission after an historical low state, while the XMM-Newton data corresponds to the average 2 – 10 keV flux level.

Taking into account the *Suzaku* results and the evident presence of iron K emission in the XMM-Newton spectra, we then investigated the presence of an emission line plus a reflection

<sup>11</sup> <http://heasarc.gsfc.nasa.gov/docs/software/xstar/xstar.html>



**Table 4.** Best-fit parameters for the the *Suzaku* (XIS+PIN, 0.6 – 70 keV) and the XMM-Newton [MOS2+pn, 0.4(1) – 10 keV] spectra of 3C 111.

Warm absorber <sup>a</sup>			Direct & reflected continua			Emission lines <sup>d</sup>			$\chi^2/\text{d.o.f.}$
$N_{\text{H}}^{\text{ion}}$ [ $10^{22} \text{ cm}^{-2}$ ]	$\log \xi$ [ $\text{erg cm s}^{-1}$ ]	$v_{\text{out}}$ [c]	$\Gamma$	$E_c$ [keV]	$R$	$E_g$ [keV]	$\sigma$ [eV]	EW [eV]	
(1)	(2)	(3)	(4)	(5)	(6)	(7)	(8)	(9)	(10)
<i>Suzaku</i>									
$69.68^{+22.59}_{-68.23}$	$5.26^{+0.59}_{-1.16}$	$0.038 \pm 0.006$	$1.61^{+0.02}_{-0.01}$	$100^{\dagger}$	$0.35 \pm 0.06$	$6.40 \pm 0.02$	$74 \pm 27$	$75 \pm 13$	$772.5/735$
						$7.06^{\dagger}$	74	12	
						$0.89 \pm 0.01$	$10^{\dagger}$	$33^{+13}_{-12}$	
<i>XMM-Newton</i> <sup>c</sup>									
–	–	–	$1.58 \pm 0.01$	$100^{\dagger}$	$0.19^{+0.05}_{-0.04}$	$6.41 \pm 0.03$	$89^{+53}_{-51}$	$38.2^{+10.7}_{-9.2}$	$1219.7/1144$
						$7.06^{\dagger}$	89	6.0	

The adopted model is a cutoff power law plus a reflection component, covered by a photoionized absorber, with the addition of the iron K complex; for the *Suzaku* data, a low-energy narrow emission line is also included. Local  $N_{\text{H}}$  are  $(1.21 \pm 0.02) \times 10^{22} \text{ cm}^{-2}$  and  $(1.04 \pm 0.01) \times 10^{22} \text{ cm}^{-2}$  for the *Suzaku* and XMM-Newton spectra, respectively. <sup>a</sup> Parametrized with an XSTAR component obtained assuming a turbulence velocity  $v_{\text{turb}} = 500 \text{ km s}^{-1}$ . <sup>b</sup> The ratio of the Fe  $K\alpha$  line and the reflection component normalizations was fixed to 0.012 (see text); the Fe  $K\beta$  and Fe  $K\alpha$  ratio line was fixed to 0.135; the Fe  $K\beta$  line width was coupled to the Fe  $K\alpha$  line width. <sup>c</sup> For the XMM-Newton spectra, the highly ionized absorber is not required by the data; the inclusion of this component implies:  $N_{\text{H}}^{\text{ion}} = 0.21^{+0.10}_{-0.08} \times 10^{22} \text{ cm}^{-2}$ ,  $\log \xi = 2.80^{+0.22}_{-0.20} \text{ erg cm s}^{-1}$ , and  $v_{\text{out}} = 0.0010 \pm 0.008 c$ . <sup>†</sup> Parameter fixed.

(1)  $N_{\text{H}}$  of the ionized absorber. (2) Ionization parameter. (3) Outflow velocity. (4) Cutoff power-law and reflection component photon index. (5) Cutoff energy. (6) Reflection fraction (calculated as the ratio of the reflection component and the direct continuum). (7) Line energy. (8) Line width. (9) Line equivalent width. (10)  $\chi^2$  and number of degree of freedom.

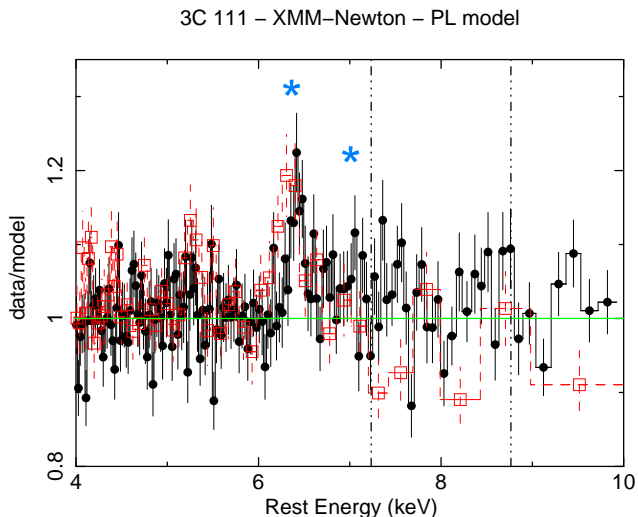


**Figure 6.** Data-to-model ratio for the XMM-Newton spectra (red open squares, MOS2; black filled circles and line, pn). The model is an absorbed power-law component ( $\Gamma \sim 1.60$ ) fitted ignoring the 5 – 7.5 keV energy band, where the iron K complex is expected. The blue stars and the vertical lines mark the position of the features detected in the XIS data, as in Fig. 2. For demonstration purposes, the data have been binned to have a significance of  $20\sigma$ .

component, the latter parametrized again with the pexrav model in XSPEC, with abundance fixed to the Solar one,  $R$  parameter fixed to 1, inclination angle fixed to  $19^\circ$ , photon index set to be equal to the slope of the cutoff power law, and energy cut-off fixed to 100 keV. As expected due to the lack of data above 10 keV, the errors on the reflection component normalization are rather high. The Fe  $K\alpha$  line parameters are:  $E = 6.41 \pm 0.03 \text{ keV}$ ,  $\sigma = 26^{+69}_{-20} \text{ eV}$ ,  $F = 1.50^{+0.64}_{-0.44} \times 10^{-5} \text{ photons cm}^{-2} \text{ s}^{-1}$ ,  $\text{EW} = 24^{+12}_{-8} \text{ eV}$  ( $\chi^2/\text{d.o.f.} = 1206.6/1143$ ). As the reflection component is poorly constrained, we again bounded its normalization to that

of the emission line. We also added a narrow Fe  $K\beta$ , bounded to the Fe  $K\alpha$  as before. Thus we obtained a best-fit parameters consistent with the *Suzaku* one: cutoff power law and reflection continuum photon index  $\Gamma = 1.58 \pm 0.01$ , reflection strength  $N_{\text{pexrav}}/N_{\text{cutoffpl}} = 0.19^{+0.05}_{-0.04}$ ,  $N_{\text{H}} = (1.04 \pm 0.01) \times 10^{22} \text{ cm}^{-2}$ . The Fe  $K\alpha$  line parameters are:  $E = 6.41 \pm 0.03 \text{ keV}$ ,  $\sigma = 89^{+53}_{-51} \text{ eV}$ ,  $F = 2.34^{+0.59}_{-0.53} \times 10^{-5} \text{ photons cm}^{-2} \text{ s}^{-1}$ ,  $\text{EW} = 38^{+11}_{-9} \text{ eV}$  with respect to the observed continuum. In particular, we note a lack of an evident response of the line to the increase in the primary emission. Clearly, with only two observations we cannot determine the time lag, or compare with the limit found with the *RXTE* monitoring by Chatterjee et al. (2011); as previously mentioned, the correlation found between X-ray flux and Fe  $K\alpha$  line intensity shows a lag less than 90 days, a result inconsistent with a torus origin for the bulk of the emission, although not with the BLR. We note that, despite the different and more complex model derived here, also in our case we found that the EW decreases with the increasing of the flux (see their fig. 8).

This model provides an acceptable description for the broad-band X-ray spectrum of 3C 111 ( $\chi^2/\text{d.o.f.} = 1219.7/1144$ ). Observed fluxes and intrinsic luminosities are summarized in Table 3; the unfolded best fit to the data is shown in Fig. 7, while the best-fit parameters are reported in Table 4.

No clear residuals in absorption at  $\sim 7 - 8 \text{ keV}$  are present. Adding an absorption line with energy and width fixed to the values previously found, we obtained for the  $E = 7.23 \text{ keV}$  and the  $E = 8.76 \text{ keV}$  an upper limit to the EW of  $-8.5 \text{ eV}$  and  $-11.1 \text{ eV}$ , respectively, formally consistent within the errors with the *Suzaku* results.

Finally, even though the previous model already provides a good description of the XMM-Newton data, taking into account the *Suzaku* results, we tested the XMM-Newton data for the presence of possible outflowing gas. When the XSTAR table previously used is applied to the XMM-Newton data, the gas parameters best-fitting the *Suzaku* spectra result to be inadequate to describe the EPIC data ( $\chi^2/\text{d.o.f.} = 1234.1/1144$ ): the lack of absorption fea-

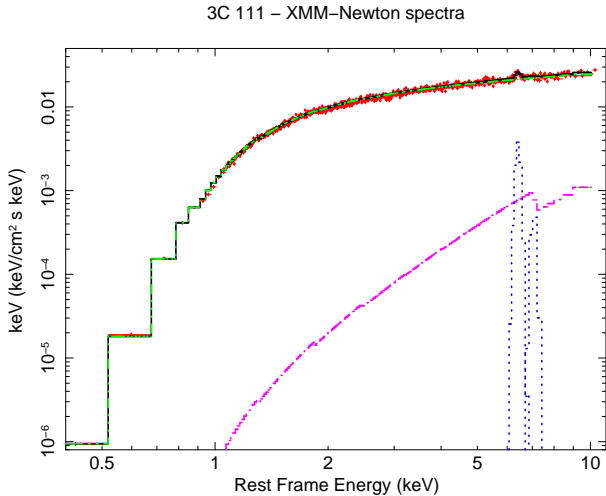


**Figure 7.** XMM-Newton EPIC spectra of 3C 111. The black lines represent the total best-fit model: the underlying continuum is modelled with a dominant cutoff power-law component (dash-dot-dot-dotted green line) plus a weak reflection component (dash-dotted magenta line). The iron K line complex is composed by a Fe  $K\alpha$  and a Fe  $K\beta$  lines (blue dotted lines). For demonstration purposes, the data have been binned to have a significance of  $20\sigma$ .

ture at high energies, in spectra with  $S/N$  good enough to detect it, may suggest that the outflowing gas has varied. To further assess the possible variability of this highly ionized absorber, we fixed its ionization and velocity to the *Suzaku* best fit values. Allowing only the column density to vary does not improve the fit; the parameter is unconstrained, with a 90% confidence interval between 0 and  $N_{\text{H}}^{\text{ion}} = 1.2 \times 10^{23} \text{ cm}^{-2}$ . This suggests again the variable nature of this disk wind. Allowing all the wind parameters to vary, a lower column density  $N_{\text{H}}^{\text{ion}} = 2.1_{-0.8}^{+1.0} \times 10^{21} \text{ cm}^{-2}$ , lower ionization parameter  $\log \xi = 2.80_{-0.20}^{+0.22} \text{ erg cm s}^{-1}$ , and zero outflow velocity  $v_{\text{out}} < 0.001 c$ , are required ( $\chi^2/\text{d.o.f.} = 1201.1/1141$ ). The improvement in the fit with respect to the model without absorber is  $\Delta\chi^2 = 18.6$  for 3 degree of freedom less. This improvement is not due to single absorption features, which are unexpected for similar values of  $\log \xi$  and  $N_{\text{H}}^{\text{ion}}$ , but instead is due to a better parameterisation of the spectral curvature due to the absorption.

#### 4.2.1 The RGS spectra

In order to investigate the emission feature at 0.8 – 0.9 keV detected by *Suzaku*, we looked at the RGS data. To increase the statistics, we also reduced and analysed the RGS data obtained in March 2001; exposure times after cleaning and count rates are reported in Table 2. As anticipated, we rebinned the RGS spectra in constant wavelength bins at twice the instrument spectral resolution ( $\Delta\lambda = 0.2 \text{ \AA}$ ) and we used the C-statistic (Cash 1979) available in XSPEC for the spectral fit: with this choice of binning, there are fewer than 20 counts per resolution bin.

A first inspection of the RGS1&2 data reveals that for both observations the spectra are background-dominated below  $\sim 0.65 \text{ keV}$ . We then considered in our analysis only data between 0.65 and 2 keV.

The two observations show a rather similar spectral shape, although with a decrease in flux of a factor of  $\sim 1.5$  (from the oldest to the most recent). In Fig. 8, *upper* and *middle panels*, we show the data/model ratio for the two observations when an absorbed power

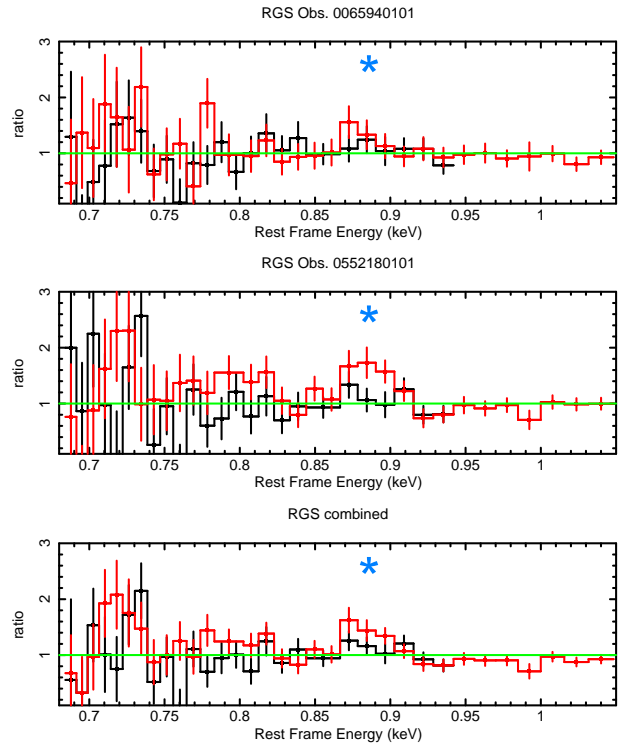


**Figure 8.** RGS background-subtracted data-to-model ratio for an absorbed power law, in the energy range 0.68 – 1.05 keV. From top to bottom, Obs. 0065940101, Obs. 0552180101, combined spectra. The blue star marks the position of the emission line at  $\sim 0.89 \text{ keV}$ .

law is applied, with  $\Gamma$  fixed to the value found for the EPIC data, 1.58 (see Sect. 4.2).

We then combined the two observations (see Fig. 8, *lower panel*). Fitting the combined spectra with the same absorbed power law, we obtained a reasonable description of the RGS continuum ( $C/\text{d.o.f.} = 171.9/105$  for 108 total bins). However, linelike residuals are present between 0.85 and 0.95 keV.

We then added to the AGN baseline continuum an unresolved line in emission, modelled with a Gaussian component; the improvement in the fit due to the addition of this component is  $\Delta C/\Delta\text{d.o.f.} = 15.2/2$ . When allowing the width to vary, the line is still unresolved. The emission line is detected at an energy of  $E = 0.890 \pm 0.002 \text{ keV}$ , with a flux of  $F = 1.43_{-0.61}^{+0.71} \times 10^{-4} \text{ photons cm}^{-2} \text{ s}^{-1}$  and an equivalent width of  $\text{EW} = 8 \pm 1 \text{ eV}$ . The line parameters from RGS1 and RGS2 are consistent within the errors.

The most likely identification of this feature is the O VIII RRC at 0.872 keV, although cannot be excluded a contribution due to the He-like triplet of Ne IX, at energies<sup>12</sup> 0.905 keV, 0.915 keV, and 0.922 keV. The quality of the data prevents us from further investigating the properties of the line.

## 5 DISCUSSION

In this paper we presented the analysis of our *Suzaku* observation of 3C 111, as well as archival unpublished XMM-Newton spectra of the BLRG.

<sup>12</sup> <http://physics.nist.gov>

The *Suzaku* and XMM-Newton emission of 3C 111 is characterized by a hard continuum, showing weak reprocessing features (iron K line and reflection component). The continuum is rather flat,  $\Gamma \sim 1.6$ , compared to the values typically found for RQ ( $\Gamma \sim 1.9$ ; e.g. Reeves & Turner 2000; Piconcelli et al. 2005; Mateos et al. 2010) and BLRGs ( $\Gamma \sim 1.7$ ; e.g. Zdziarski & Grandi 2001; Grandi, Malaguti, & Fiacchi 2006). The broad-band shape observed by *Suzaku* and XMM-Newton is in good agreement; the 0.5 – 10 keV flux changes of a factor 2.5 in the 6 months separating the two observations. Such a strong flux variability is not surprising in this source. The power spectral density analysis of the *RXTE* monitoring between 2.4 and 10 keV presented by Chatterjee et al. (2011) reveals a break timescale of  $\sim 13$  days; flares as strong as a factor of 2 – 3 in flux are observed in  $\sim 1$  month. Previous XMM-Newton and *RXTE* observations caught the source in a higher flux state than *Suzaku* (by a factor of 3 in the 2 – 10 keV energy range) as well as in the new XMM-Newton data. Again, the X-ray spectral shape does not change significantly:  $\Gamma \sim 1.63 - 1.75$ ,  $R \lesssim 0.3$  (Lewis et al. 2005). Variations in the intensity of the emission are observed up to at least  $\sim 100$  keV, as implied by the comparison between the HXD-PIN emission and the BAT averaged spectrum. Despite the continuum variation, the fluxes of the 6.4 keV Fe K $\alpha$  line, clearly detected in both XMM-Newton and *Suzaku* datasets, are consistent.

### 5.1 Emission and absorption features

In addition to the Fe K $\alpha$ -Fe K $\beta$  complex, the most significant features detected in the XIS spectra are two absorption lines at  $E \sim 7.24$  and  $\sim 8.77$  keV, respectively. The presence of such absorption features are not unique to 3C 111: an analysis of 5 nearby, X-ray bright BLRGs shows that these absorption lines are detected in 60% of the sources (Tombesi et al. 2010b, where a detailed analysis of these features is discussed). Their likely interpretation as blue-shifted iron K lines implies an origin from highly ionized gas outflowing with  $v_{\text{out}} \sim 0.04 c$ , probably related with accretion disk winds/outflows. From the ionization parameter  $\xi \equiv L_{\text{ion}}/(nR^2)$  and the column density of the outflowing gas, under the reasonable assumption of thickness of the clouds  $\Delta R = N_{\text{H}}/n$  lower than the distance,  $\Delta R \ll R$ , we can estimate the launch radius. Adopting the absorption-corrected ionizing luminosity between 0.0136 keV and 13.6 keV as obtained from the *Suzaku* data ( $2.5 \times 10^{44}$  ergs s $^{-1}$ ), we found a sub-parsec distance from the central BH,  $R < 9 \times 10^{15}$  cm.

Assuming the mean black hole mass estimated by Chatterjee et al. (2011),  $M_{\text{BH}} = 1.8 \times 10^8 M_{\odot}$ , the escape velocity at this radius is a factor 2 higher than the outflow velocity,  $v_{\text{esc}} \sim 0.077 c$ . The highest black hole mass estimated for 3C 111,  $M_{\text{BH}} = 3.6 \times 10^9 M_{\odot}$  (Marchesini, Celotti, & Ferrarese 2004, see Table 1), would imply an even worse situation, with an escape velocity a factor 10 higher than  $v_{\text{out}}$ . The outflow is then unable to escape from the central region where is produced, and the absorber is most likely unstable. Indeed, at the time of the XMM-Newton observation the outflowing gas has varied. No absorption features are detected in the EPIC spectra. Testing a photoionized absorber as seen in the *Suzaku* data, we found a steady absorber with lower column density and lower ionization parameter.

Finally, the XIS spectra also show an emission feature at  $\sim 0.9$  keV; the most commonly observed features at energies around  $E = 0.89 \pm 0.01$  keV are the O VIII RRC at 0.872 keV or the Ne IX triplet lines at 0.905 keV, 0.915 keV, and 0.922 keV; at the XIS resolution these features are unresolved. An emission line is also detected in the combined RGS spectra of 3C 111, with con-

**Table 5. Spectral indices and fluxes from the combined fit to the X-ray SED.**

Satellite (Year)	$\Gamma$	Flux <sup>a</sup> [ $10^{-11}$ ergs cm $^{-2}$ s $^{-1}$ ]	
		0.5 – 10 keV	10 – 200 keV
<i>BeppoSAX</i> (1998)	$1.67 \pm 0.06$	2.84	7.42
XMM-Newton (2001)	$1.68 \pm 0.01$	7.43	15.78
<i>Swift</i> (58-month)	$1.57 \pm 0.09$	3.90	11.41
<i>Suzaku</i> (2008)	$1.61 \pm 0.01$	2.22	6.89
<i>INTEGRAL</i> (2008)	$0.95^{+0.43}_{-0.40}$	1.08	12.35
XMM-Newton (2009)	$1.61 \pm 0.01$	5.45	14.05

Errors are quoted at the 90% confidence level for 1 parameter of interest ( $\Delta\chi^2 = 2.71$ ). <sup>a</sup> Observed fluxes.

sistent energy,  $E = 0.890 \pm 0.002$  keV. The measured fluxes are consistent within the errors:  $1.43^{+0.71}_{-0.61} \times 10^{-4}$  photons cm $^{-2}$  s $^{-1}$  and  $2.09^{+0.88}_{-0.85} \times 10^{-4}$  photons cm $^{-2}$  s $^{-1}$  for XMM-Newton and *Suzaku*, respectively. Similar features, produced by photoionized gas, have been detected in two other FR II radio galaxies, the BLRG 3C 445 (e.g. Grandi et al. 2007; Sambruna, Reeves, & Braito 2007) and the NLRG 3C 234 (Piconcelli et al. 2008).

### 5.2 From X-ray to $\gamma$ -ray

The comparison presented here between HXD-PIN emission and the BAT averaged spectrum at high energies, and XMM-Newton and XIS data at lower energies, confirms the strong variability of 3C 111, which could be tentatively ascribed to the jet variability. Only broad-band monitoring observations will allow us to confirm or rule out this possibility. No clear roll-over is detected in the *Suzaku* data, which can be explained by the presence of such a jet component. Indeed, if the GSO detection is robust, there is a marginal evidence of the emerging of a jet component at energies higher than 10 keV, although the present data do not allow us to firmly establish its relative contribution with respect to the primary continuum. The strong variability observed in the X-ray flux together with the flat photon index of the continuum, could suggest dilution of the disk emission due to a variable jet contribution. In principle, data with higher spatial resolution could allow us to investigate the jet contribution below 10 keV, resolving some knots that are blended for XMM-Newton (and even more for *Suzaku*); indeed, X-ray jet emission may arise on a range of scales, as the one-sided radio jet is detected at mas to arc-minutes. However, images from a *Chandra* observation (Hogan et al. 2011) show that all but one the visible knots along the jet fall outside the extraction region of the XMM-Newton spectra, and none of them is bright enough to be detected in the automatic source detection and analysis performed with XASSIST<sup>13</sup>. The lack of unresolved bright knots in the XMM-Newton spectra, that correspond to a higher flux level, make unlikely that the variation is jet-related.

In the  $\gamma$ -ray band, an *Egret* identification of 3C 111 as a  $\gamma$ -ray source has been suggested, although with some debate on the real contribution of 3C 111 to the total  $\gamma$ -ray emission of the *Egret* counterpart (Sguera et al. 2005; Hartman, Kadler, & Tueller 2008). Recently, an association with a *Fermi* source has been reported by Abdo et al. (2010). The fluxes detected in the  $\gamma$ -ray band are:  $F_{0.75-3 \text{ MeV}} < 4.2 \times 10^{-10}$  ergs cm $^{-2}$  s $^{-1}$  and  $F_{3-30 \text{ MeV}} <$

<sup>13</sup> <http://xassist.pha.jhu.edu/zope/xassist>

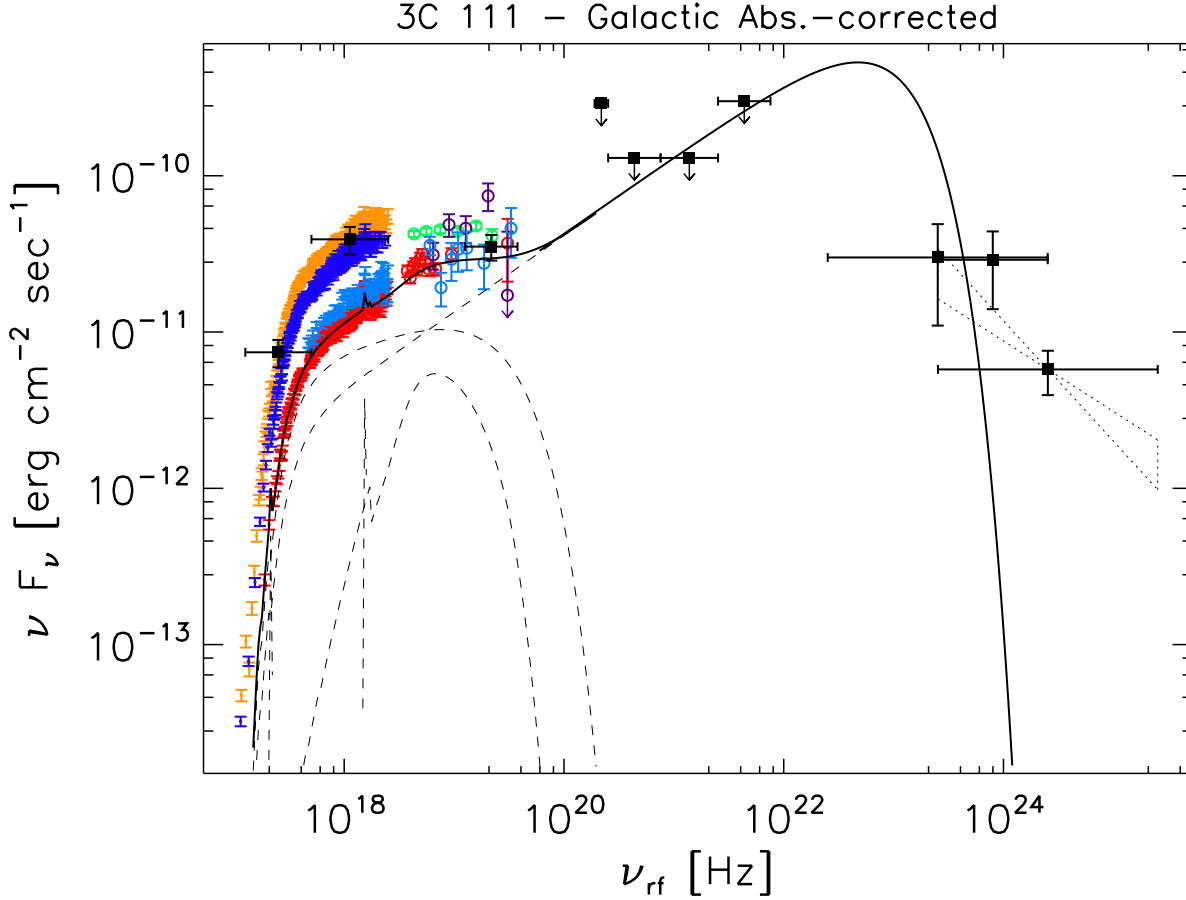


**Figure 9.** Rest-frame high-energy SED of 3C 111. Red symbols are *Suzaku* spectra (XIS03, PIN, and GSO); above  $10^{18}$  Hz, green and purple circles are BAT and INTEGRAL data, respectively. *BeppoSAX* MECS and PDS spectra are plotted in light blue; orange symbols are XMM-*Newton* MOS data from 2001, while blue spectrum is the XMM-*Newton* MOS2 spectrum analysed in this paper. Black filled squares are taken from literature (Hartman, Kadler, & Tueller 2008; Abdo et al. 2010): from low to high energies, *ASCA*, *CGRO* (*OSSE*, *COMPTEL*, and *Egret* instruments), and *Fermi* data. Data are corrected for local absorption. Dashed black lines are the components of the best-fit model for the *Suzaku* data when the jet component is included; the solid line corresponds to the total model, with a cut off at  $\sim 10$  MeV applied.

$4.3 \times 10^{-10}$  ergs  $\text{cm}^{-2} \text{s}^{-1}$  (*COMPTEL*), and  $F_{0.1-10\text{GeV}} \sim 3 \times 10^{-11}$  ergs  $\text{cm}^{-2} \text{s}^{-1}$  [*Egret*, both on-board the *Compton Gamma Ray Observatory* (*CGRO*); Hartman, Kadler, & Tueller 2008];  $F_{1-100\text{GeV}} \sim 6 \times 10^{-12}$  ergs  $\text{cm}^{-2} \text{s}^{-1}$  (*Fermi*; Abdo et al. 2010). These fluxes are highly above the value predicted by the best-fit model to the 0.6 – 70 keV *Suzaku* data without a jet component. This supports the hypothesis of high-energy emission due to the jet in 3C 111. Recently, Kataoka et al. (2011) ascribed the *Fermi* detection to a pc-scale relativistic emission from the jet. Extrapolating the dual power law model, including a possible jet component (see Sect. 4.1), to high energies, we found for the jet component  $F_{3-30\text{MeV}}^{\text{jet}} = 4.9 \times 10^{-10}$  ergs  $\text{cm}^{-2} \text{s}^{-1}$ . Taking into account the typical variability of jet emission, this flux is in substantial agreement with the upper limits obtained in the *COMPTEL* energy range. Qualitatively, a peak at  $\sim 100$  MeV would cause the observed jet component to be compatible with the observed emission above 0.1 GeV.

This is evident looking at Fig. 9, where we present the high-energy historical SED for 3C 111 from X-ray to  $\gamma$ -ray energies. We used the *Suzaku*, XMM-*Newton*, and *Swift* observations analysed in this paper together with *ASCA*, XMM-*Newton* MOS (from 2001), *BeppoSAX* (from 1998), *INTEGRAL* (from 2008), *CGRO*,

and *Fermi* data. For safe of clarity, in Fig. 9 we do not show XIS1 and pn (from 2009) data. We note that the *Swift* spectrum is averaged over more than 4 years. The strong variability previously mentioned is clearly evident when all the datasets are plotted together. In order to understand the driver of the variability, we fitted all the datasets together, adopting the best-fit continuum model of the *Suzaku* data, i.e. an absorbed cutoff power law plus a reflection component and the iron K complex; since the comparison between *Suzaku* and XMM-*Newton* spectra shows that the lines do not vary with the continuum, we fixed the reprocessing features to the best fit value found for *Suzaku*.

As a first step, we allowed only the relative normalization of the primary power law to vary between the observations. For observations extending down to a few keV, also the column density was allowed to vary. This fit already provides a reasonable representation of the SED ( $\chi^2/\text{d.o.f.} = 3177.6/2429$ ), our aim being to investigate the variations in the main spectral properties (continuum slope and emission intensity), and not to find a detailed description of all the spectra. However, to further investigate the observed variability, we also allowed the power-law photon index to vary; the observed change of intensity and spectral shape is summarized in Table 5 ( $\chi^2/\text{d.o.f.} = 2972.8/2423$ ). We obtained rather similar values

of the photon index, spanning a range from  $\Gamma = 1.57 \pm 0.09$  (*Swift*) to  $\Gamma = 1.68 \pm 0.01$  (*XMM-Newton* from 2001). The only outlier is the *INTEGRAL* observation, for which we obtain  $\Gamma = 0.95^{+0.43}_{-0.40}$ . This is probably due to the low quality of the data, confirmed by the poor constraints to the value of  $\Gamma$ , coupled with the high-energy cutoff applied,  $E_c = 100$  keV. Fitting the data with a simple power law would increase a little the best-fit value of the photon index, although with strong residuals at the high-energy end of the spectrum. The column density varies between  $\sim 1.08 \times 10^{22} \text{ cm}^{-2}$  (*XMM-Newton* from 2009) and  $\sim 1.50 \times 10^{22} \text{ cm}^{-2}$  (*BeppoSAX* from 1998). As noted before, we observe significant variability in the 0.5 – 10 keV flux, from  $\sim 2.8 \times 10^{-11} \text{ ergs cm}^{-2} \text{ s}^{-1}$  (our XIS data) to  $\sim 7.4 \times 10^{-11} \text{ ergs cm}^{-2} \text{ s}^{-1}$  (*XMM-Newton* from 2001). At higher energies, the stronger variation is observed between the *Suzaku* and the *XMM-Newton* (from 2001) data.

This analysis shows that a brightening of the source does not imply a flatter power law, thus suggesting that the main driver of the increase in the flux may not be a strong increase in the jet component. Although our analysis is limited by the number of spectra, we note that the photon indices are well constrained thanks to the use of soft X-ray data as well as data above 10 keV. After excluding the *INTEGRAL* point, the change in slope with the flux found here, adopting a more complex model, is marginally consistent with that obtained from the *RXTE* monitoring (Chatterjee et al. 2011, see their fig. 8), which shows a similar trend albeit with a larger  $\Delta\Gamma$  and covering a large range in the 2 – 10 keV flux.

In our observational program, we have BLRGs showing a spread of the jet angle with respect to the line of sight. Despite the strong uncertainties in the orientation, the closest candidate to be compared to 3C 111 is 3C 382. Recently, from high-quality *Suzaku* data Sambruna et al. (2011) estimated for this BLRG a disk inclination of  $\sim 25^\circ - 30^\circ$ ; at bigger scales, radio observations found a lower limit to the inclination angle of  $\sim 15^\circ$  (Eracleous & Halpern 1998). The best estimate of the jet inclination for 3C 111 is  $\sim 19^\circ$ , with a proposed range of  $10^\circ < i < 26^\circ$  (Kadler et al. 2008; Lewis et al. 2005). Despite this similarity, the X-ray emission of the two sources is remarkably different, with 3C 382 showing an X-ray spectrum more similar to that observed from Seyfert galaxies. This implies that the relative importance of the jet is not related only to geometrical properties (i.e., orientation with respect to the line of sight). Different velocities, or a bent jet, can play an important role.

Finally, the X-ray emission of 3C 111 appears significantly different from that of a typical Seyfert galaxy in many aspects, e.g. flatter intrinsic emission and weak reflection features. On the other hand, its time variability shows properties that correlate with the black hole mass, following the same scaling law observed in stellar-mass black hole X-ray binaries and Seyfert galaxies, suggesting that a similar accretion process is powering these different systems (Chatterjee et al. 2011). It is worth noting the large dispersion of intrinsic X-ray properties shown by RL AGN (Sambruna et al. 2009, and references therein), similar to the one found out for the RQ sources. The overlapping of the distributions of photon index and reflection features observed in both classes supports the idea of common accretion structure, with a second parameter in addition to the accretion rate that determines the jet production efficiency. The most likely candidate is the black hole spin, although how does it works in producing the observed RLs-RQs dichotomy, or the FRIs-FRIIs division, is still strongly debated (e.g., the “spin paradigm” coupled with intermittent jet activity, Sikora, Stawarz, & Lasota 2007; or the “gap paradigm”, Garofalo 2009; Garofalo, Evans, & Sambruna 2010). In particular, in the

heuristic scenario proposed by Garofalo et al., collimated jets coupled with intermediate accretion efficiency, as observed in 3C 111 (see Table 1), can occur for retrograde systems. This configuration also implies a larger size of the gap region between the inner edge of accretion disks and the black hole horizon, size that is connected to the energetics of the disk itself. The weakness of reflection features is a natural consequence of such a configuration; moreover, larger gap regions can limit the presence of disk winds (Kuncic & Bicknell 2004, 2007). Unstable outflows, weaker than in RQ AGN, could be therefore compatible with High Excitation FRII states, such in 3C 111 (Buttiglione et al. 2010), while at the extreme end, radiatively inefficient accretion flows in Low Excitation Radio Galaxies ( $L/L_{\text{Edd}} \sim 10^{-(5-7)}$ ) might inhibit the launch of disk winds.

## 6 SUMMARY

In this paper we presented the X-ray spectra of 3C 111, obtained with *Suzaku* as part of our observational program devoted to study the high-energy emission of the brighter BLRGs. A recent *XMM-Newton* observation of  $\sim 120$  ksec is analysed as well.

The 3C 111 emission extends up to  $\sim 200$  keV, with a rather flat continuum; in spite of this, no signatures of jet emission are visible below 10 keV. *Suzaku* observed the source at a minimum flux level, as shown by the *RXTE* monitoring. In the 6 months separating the *Suzaku* and *XMM-Newton* observations, the flux increases by a factor of 2.5, a level of variability which is not unexpected in this source. We confirm the weakness of the reflection features, as found in previous observations. An iron K complex is clearly detected in both datasets, with a rather low EW. The intensities of the line detected by *XMM-Newton* and *Suzaku* are consistent, with a lack of immediate response of the line properties to the continuum variation. In addition to the iron K complex, absorption features due to a highly ionized, ultra-fast, nuclear outflowing gas are detected in the XIS data. At the time of the *XMM-Newton* observation, the gas has varied: adopting the photoionized absorber as seen in the *Suzaku* data, then a lower column density and lower ionization state are required. Both XIS data and RGS spectra show the presence of a narrow line at  $\sim 0.89$  keV, which is most likely identified with either the O VIII RRC or the Ne IX triplet lines.

The lack of detection of a roll-over in the primary emission is probably due to the appearance of the jet as a dominant component in the hard X-ray band, as suggested by the detection with the GSO on-board *Suzaku* above  $\sim 100$  keV. From a qualitative point of view, the emission observed by *Egret* and *Fermi* above 0.1 GeV is compatible with such a jet component assuming that this peaks at energies of  $\sim 100$  MeV. If the detection is confirmed, the emergence of a jet component can explain differences observed in the high-energy emission of BLRGs similar in other aspects. The relative importance of the jet component is not simply related to the system inclination, but can be associated to the velocity of the jet; a change of the opening angle of the jet passing from the nuclear region, where the observed X-ray emission is produced, to the most distant regions, where the radio emission is observed, may also play a role.

Finally, we presented the high-energy historical SED for 3C 111, from X-ray to  $\gamma$ -ray. Our qualitative analysis suggests that the strong variability observed for 3C 111 is probably driven by a change in the primary continuum. This implies that simultaneous broad-band X-ray and  $\gamma$ -ray monitoring is needed to unambiguously constrain the parameters of the disk-jet system, and correctly

understand the contribution of the different components (i.e., disk emission, reflection, jet) to the total emission.

## ACKNOWLEDGMENTS

This research has made use of data obtained from the High Energy Astrophysics Science Archive Research Center (HEASARC), provided by NASA's Goddard Space Flight Center, and of the NASA/IPAC Extragalactic Database (NED) which is operated by the Jet Propulsion Laboratory, California Institute of Technology, under contract with the National Aeronautics and Space Administration. Based on observations obtained from the *Suzaku* satellite, a collaborative mission between the space agencies of Japan (JAXA) and the USA (NASA), and with *XMM-Newton* (an ESA science mission with instruments and contributions directly funded by ESA Member States and the USA, NASA). We warmly thank the referee for her/his suggestions that significantly improved the paper. We are grateful to M. Ceballos, R. Saxton and S. Sembay for their help in handling the *XMM-Newton* data problems. We warmly thank V. Bianchin for reducing the *INTEGRAL* data. R.M.S. acknowledges support from NASA through the *Suzaku* program. V.B. acknowledges support from the UK STFC research council. L.B. acknowledges support from the Spanish Ministry of Science and Innovation through a "Juan de la Cierva" fellowship. Financial support for this work was provided by the Spanish Ministry of Science and Innovation, through research grant AYA2009-08059.

## REFERENCES

- Abdo A. A., et al., 2010, *ApJ*, 715, 429  
 Antonucci R., 1993, *ARA&A*, 31, 473  
 Ballantyne D. R., 2007, *MPLA*, 22, 2397  
 Ballantyne D. R., Ross R. R., Fabian A. C., 2002, *MNRAS*, 332, L45  
 Blandford R. D., Znajek R. L., 1977, *MNRAS*, 179, 433  
 Blandford R. D., Payne D. G., 1982, *MNRAS*, 199, 883  
 Blustin A. J., Page M. J., Fuerst S. V., Branduardi-Raymont G., Ashton C. E., 2005, *A&A*, 431, 111  
 Boldt E., 1987, *PhR*, 146, 215  
 Braito V., Reeves J. N., Sambruna R. M., Gofford J., 2011, *MNRAS*, 581  
 Buttiglione S., Capetti A., Celotti A., Axon D. J., Chiaberge M., Macchetto F. D., Sparks W. B., 2010, *A&A*, 509, A6  
 Cash W., 1979, *ApJ*, 228, 939  
 Chatterjee R., et al., 2011, *ApJ*, 734, 43  
 Creshaw D. M., Kraemer S. B., George I. M., 2003, *ARA&A*, 41, 117  
 Dadina M., 2007, *A&A*, 461, 1209  
 Daly R. A., 2009, *ApJ*, 696, L32  
 Daly R. A., 2009, *ApJ*, 691, L72  
 den Herder J. W., et al., 2001, *A&A*, 365, L7  
 Eracleous M., Halpern J. P., 2003, *ApJ*, 599, 886  
 Eracleous M., Halpern J. P., 1998, *ApJ*, 505, 577  
 Eracleous M., Halpern J. P., 1994, *ApJS*, 90, 1  
 Eracleous M., Sambruna R., Mushotzky R. F., 2000, *ApJ*, 537, 654  
 Fender R. P., Gallo E., Russell D., 2010, *MNRAS*, 406, 1425  
 Garofalo D., Evans D. A., Sambruna R. M., 2010, *MNRAS*, 406, 975  
 Garofalo D., 2009, *ApJ*, 699, 400  
 George I. M., Fabian A. C., 1991, *MNRAS*, 249, 352  
 Grandi P., Guainazzi M., Cappi M., Ponti G., 2007, *MNRAS*, 381, L21  
 Grandi P., Malaguti G., Fiocchi M., 2006, *ApJ*, 642, 113  
 Grandi P., Urry C. M., Maraschi L., 2002, *NewAR*, 46, 221  
 Hardcastle M. J., Evans D. A., Croston J. H., 2007, *MNRAS*, 376, 1849  
 Hartman R. C., Kadler M., Tueller J., 2008, *ApJ*, 688, 852  
 Hogan B. S., Lister M. L., Kharb P., Marshall H. L., Cooper N. J., 2011, *ApJ*, 730, 92  
 Kadler M., et al., 2008, *ApJ*, 680, 867  
 Kalberla P. M. W., Burton W. B., Hartmann D., Arnal E. M., Bajaja E., Morras R., Pöppel W. G. L., 2005, *A&A*, 440, 775  
 Kallman T., Bautista M., 2001, *ApJS*, 133, 221  
 Kallman T. R., Palmeri P., Bautista M. A., Mendoza C., Krolik J. H., 2004, *ApJS*, 155, 675  
 Kataoka J., et al., 2011, *arXiv*, arXiv:1107.3370  
 Kokubun M., et al., 2007, *PASJ*, 59, 53  
 Koyama K., Uchiyama H., Hyodo Y., Matsumoto H., Tsuru T. G., Ozaki M., Maeda Y., Murakami H., 2007, *PASJ*, 59, 237  
 Kuncic Z., Bicknell G. V., 2004, *ApJ*, 616, 669  
 Kuncic Z., Bicknell G. V., 2007, *Ap&SS*, 311, 127  
 Lewis K. T., Eracleous M., Gliozzi M., Sambruna R. M., Mushotzky R. F., 2005, *ApJ*, 622, 816  
 Linfield R., Perley R., 1984, *ApJ*, 279, 60  
 McKernan B., Yaqoob T., Reynolds C. S., 2005, *MNRAS*, 361, 1337  
 McKernan B., Yaqoob T., Reynolds C. S., 2004, *ApJ*, 617, 232  
 McKernan B., Yaqoob T., Mushotzky R., George I. M., Turner T. J., 2003, *ApJ*, 598, L83  
 Magdziarz P., Zdziarski A. A., 1995, *MNRAS*, 273, 837  
 Marchesini D., Celotti A., Ferrarese L., 2004, *MNRAS*, 351, 733  
 Mateos S., et al., 2010, *A&A*, 510, A35  
 Matt G., Fabian A. C., Reynolds C. S., 1997, *MNRAS*, 289, 175  
 Matt G., Fabian A. C., Ross R. R., 1996, *MNRAS*, 278, 1111  
 Nandra K., George I. M., 1994, *MNRAS*, 267, 974  
 Ness, J.-U., (Revision editor) & ESA: *XMM-Newton* SOC 2010, "XMM-Newton Users Handbook", Issue 2.8.1  
[http://xmm.esac.esa.int/external/xmm\\_user\\_support/documentation/uhb/XMM\\_UHB.html](http://xmm.esac.esa.int/external/xmm_user_support/documentation/uhb/XMM_UHB.html)  
 Nilsson K., Valtonen M. J., Kotilainen J., Jaakkola T., 1993, *ApJ*, 413, 453  
 Palmeri P., Mendoza C., Kallman T. R., Bautista M. A., Meléndez M., 2003, *A&A*, 410, 359  
 Piconcelli E., Bianchi S., Miniutti G., Fiore F., Guainazzi M., Jimenez-Bailon E., Matt G., 2008, *A&A*, 480, 671  
 Piconcelli E., Jimenez-Bailón E., Guainazzi M., Schartel N., Rodríguez-Pascual P. M., Santos-Lleó M., 2005, *A&A*, 432, 15  
 Protassov R., van Dyk D. A., Connors A., Kashyap V. L., Siemiginowska A., 2002, *ApJ*, 571, 545  
 Reeves J. N., Turner M. J. L., 2000, *MNRAS*, 316, 234  
 Reeves G. D., Henderson M. G., Koller J., Chen Y., Friedel R. H., Zaharia S. G., Thomsen D., 2009, *AGUFMSA43*, A1623  
 Reeves J. N., Gofford J., Braito V., Sambruna R., 2010, *ApJ*, 725, 803  
 Ross R. R., Fabian A. C., Young A. J., 1999, *MNRAS*, 306, 461  
 Ross R. R., Fabian A. C., 2005, *MNRAS*, 358, 211  
 Sambruna R. M., et al., 2009, *ApJ*, 700, 1473  
 Sambruna R. M., Tombesi F., Reeves J. N., Braito V., Ballo L., Gliozzi M., Reynolds C. S., 2011, *ApJ*, 734, 105  
 Sambruna R. M., Reeves J. N., Braito V., 2007, *ApJ*, 665, 1030

- Sambruna R. M., Eracleous M., Mushotzky R. F., 2002, *NewAR*, 46, 215
- Sguera V., Bassani L., Malizia A., Dean A. J., Landi R., Stephen J. B., 2005, *A&A*, 430, 107
- Sikora M., Stawarz Ł., Lasota J.-P., 2007, *ApJ*, 658, 815
- Spergel D. N., et al., 2007, *ApJS*, 170, 377
- Spergel D. N., et al., 2003, *ApJS*, 148, 175
- Strüder L., et al., 2001, *A&A*, 365, L18
- Takahashi T., et al., 2007, *PASJ*, 59, 35
- Tchekhovskoy A., Narayan R., McKinney J. C., 2010, *ApJ*, 711, 50
- Tombesi F., Sambruna R. M., Reeves J. N., Braitto V., Ballo L., Gofford J., Cappi M., Mushotzky R. F., 2010, *ApJ*, 719, 700
- Tombesi F., Cappi M., Reeves J. N., Palumbo G. G. C., Yaqoob T., Braitto V., Dadina M., 2010, *A&A*, 521, A57
- Torresi E., Grandi P., Longinotti A. L., Guainazzi M., Palumbo G. G. C., Tombesi F., Nucita A., 2010, *MNRAS*, 401, L10
- Turner T. J., Miller L., 2009, *A&ARv*, 17, 47
- Turner M. J. L., et al., 2001, *A&A*, 365, L27
- Urry C. M., Padovani P., 1995, *PASP*, 107, 803
- Vermeulen R. C., Cohen M. H., 1994, *ApJ*, 430, 467
- Wilms J., Allen A., McCray R., 2000, *ApJ*, 542, 914
- Yaqoob T., Murphy K. D., Miller L., Turner T. J., 2010, *MNRAS*, 401, 411
- Zdziarski A. A., Grandi P., 2001, *ApJ*, 551, 186